PORE PRESSURE ESTIMATION FOR SHALY SAND FORMATIONS USING ROCK PHYSICS MODELS FOR COMPRESSIONAL AND SHEAR VELOCITIES: A 1D GEOMECHANICAL APPROACH

(ESTIMATIVA DA PRESSÃO DE POROS EM ARENITOS ARGILOSOS UTILIZANDO MODELOS DE FÍSICA DE ROCHA PARA VELOCIDADES COMPRESSIONAIS E CISALHANTES: UM ENFOQUE GEOMECÂNICO 1D)

RENZO FRANCIA MIMBELA

UNIVERSIDADE ESTADUAL DO NORTE FLUMINENSE
LABORATÓRIO DE ENGENHARIA E EXPLORAÇÃO DE PETRÓLEO

MACAÉ - RJ
JULHO – 2021

FICHA CATALOGRÁFICA PREPARADA PELA BIBLIOTECA DO LENEP

622.338282	
F817p	Francia Mimbela, Renzo Rigo
2021	Pore pressure estimation for shaly sand formations using rock physics models for compressional and shear velocities: a 1D geomechanical approach (Estimativa da pressão de poros...) / Renzo Rigo Francia Mimbela. --- Macaé: Universidade Estadual do Norte Fluminense Darcy Ribeiro. Laboratório de Engenharia e Exploração de Petróleo, 2021.
	xiv, 73f. : il
	Tese (Doutorado em Engenharia de Reservatório e de Exploração)
	Orientador: Fernando Sergio de Moraes.
	Bibliografia: f. 69-73
	1. Pressão de poro 2. Eaton 3. Geomecânica 4. Geopressões 5. Inversão não linear I. Título.

PORE PRESSURE ESTIMATION FOR SHALY SAND FORMATIONS USING ROCK PHYSICS MODELS FOR COMPRESSIONAL AND SHEAR VELOCITIES: A 1D GEOMECHANICAL APPROACH

(ESTIMATIVA DA PRESSÃO DE POROS EM ARENITOS ARGILOSOS UTILIZANDO MODELOS DE FÍSICA DE ROCHA PARA VELOCIDADES COMPRESSIONAIS E CISALHANTES: UM ENFOQUE GEOMECÂNICO 1D)

RENZO FRANCIA MIMBELA

A thesis presented to the Science and Technology Center of the North Fluminense State University as a pre-requisite to obtain the Doctor Degree in Reservoir and Exploration Engineering (D.Sc), with emphasis on Integrated Reservoir Modelling.

Advisor: Prof. Fernando Sergio de Moraes

MACAÉ - RJ

JULHO – 2021

PORE PRESSURE ESTIMATION FOR SHALY SAND FORMATIONS USING ROCK PHYSICS MODELS FOR COMPRESSIONAL AND SHEAR VELOCITIES: A 1D GEOMECHANICAL APPROACH

(ESTIMATIVA DA PRESSÃO DE POROS EM ARENITOS ARGILOSOS UTILIZANDO MODELOS DE FÍSICA DE ROCHA PARA VELOCIDADES COMPRESSIONAIS E CISALHANTES: UM ENFOQUE GEOMECÂNICO 1D)

RENZO FRANCIA MIMBELA

A thesis presented to the Science and Technology Center of the North Fluminense State University as a pre-requisite to obtain the Doctor Degree in Reservoir and Exploration Engineering (D.Sc), with emphasis on Integrated Reservoir Modelling.

Approved in 22/07/2021
Examining Committee:

Irineu de Azevedo Lima Neto

Irineu de Azevedo Lima Neto (D.Sc., Reservatórios – FACC)

Marco Ceia

Marco Antônio Rodrigues de Ceia (D.Sc., Reservatórios – LENEP/CCT/UENF)

Luiz Alberto Santos (D.Sc., E. Civil – PETROBRAS/UFF)

Fernando S. de Moraes

Fernando Sergio de Moraes (Ph.D., Geofísica – LENEP/CCT/UENF)
(Advisor)

To God.

To my family...

ACKNOWLEDGMENTS

First, I would like to express my gratitude to God and my family for always being so loving and understanding.

To my advisor, professor Fernando Sergio de Moraes, for his support over the last four years. Thank you for the support with excellent technical discussions, and thank you most for having trusted me.

To PETROBRAS for the financial support through a research grant (TC 5850.0108361.18.9) and the PFRH-PB 226 Graduate Program in Applied Geophysics. We also thank the Conselho Nacional de Desenvolvimento Científico e Tecnológico (CNPq) for the financial support of the INCT-GP and Coordenação de Aperfeiçoamento de Pessoal de Nível Superior - Brasil (CAPES) - Finance Code 001, for the institutional and financial support of the Graduate Program in Exploration and Reservoir Engineering.

To Vizeu Santos for his support in the implementation of the anisotropy inversion algorithm.

Thanks also to UENF-LENEP for conceding me the possibility to participate in the Doctoring course of petroleum engineering and exploration.

TABLE OF CONTENTS

ABSTRACT

Pore pressure estimation in sedimentary basins has been made exclusively through the compressional velocity data since the 1960s, using the normal compaction trend and lithostatic pressure profile derived from wireline logs. Considering that seismic velocity is highly dependent on petrophysical parameters such as porosity and lithology, pore pressure estimation is commonly associated with a high degree of uncertainty due to simplistic assumptions that neglect those dependencies. To improve that, we propose two empirical velocity models based on compressional and shear rock physics relations for pore pressure prediction in shaly sand formations. These formulations extend Bowers and Doyen formulae, linking compressional velocities with effective stress and petrophysical parameters. Applications of such relations accounting for porosity, shale content, and saturation variations require integrated investigations at the core and well-log scales to accurately represent and model seismic velocities, which have been included in this thesis as a three-part development. First, I discuss rock physics model sensitivity to lithology, fluid and pressure variations using synthetic laboratory ultrasonic measurements of seismic velocities. Then I deal with the problem that compressional and shear wave sonic velocities measured in deviated wells can be highly affected by VTI anisotropy, generally requiring corrections for this effect. Anisotropic modeling and inversion on synthetic sonic log show the magnitude of the effect and that it can be efficiently corrected by the proposed method. Finally, I use a nonlinear multidimensional inversion approach to calibrate the proposed models and apply them in the context of a 1D geomechanics and pore pressure prediction study of an upper cretaceous overpressured shaly sand oil reservoir. The results show good agreement with pore pressure data and pressure predictions from the traditional Eaton method. The advantage of the proposed approach is its consistency throughout the entire well-log petrophysical interpretation workflow, especially concerning porosity, shale volume and saturation.

Keywords: Pore pressure, overpressure mechanism, rock physics, 1D geomechanics, Eaton method, Bowers method, nonlinear inversion.

RESUMO

A estimativa da pressão de poros em bacias sedimentares tem sido feita exclusivamente através dos dados da velocidade compressional desde 1960, usando o *trend* de compactação normal e o perfil de pressão litostática derivado de perfis a cabo. Considerando que a velocidade sísmica é altamente dependente de parâmetros petrofisicos, como porosidade e litologia, a estimativa de pressão de poro é comumente associada a um alto grau de incerteza devido a suposições simplistas que negligenciam essas dependências. Para mitigar estas incertezas, proponho dois modelos empíricos em função das velocidades e baseados nas relações físicas da onda compressional e cisalhante para a previsão da pressão de poros em formações areio-argilosas. Essas formulações estendem as fórmulas de Bowers e Doyen, vinculando as velocidades com a tensão efetiva e parâmetros petrofisicos. As aplicações de tais relações empíricas envolvendo variações de porosidade, conteúdo de argila e saturação requerem investigações integradas nas escalas de amostras e perfis do poço para representar e modelar com precisão as velocidades sísmicas, incluídas nesta tese como um desenvolvimento em três partes. Primeiro, discuto a modelagem de física de rochas e a substituição de fluidos utilizando medidas laboratórais sintéticas de velocidades ultrassônicas. Em seguida, lido com o problema de que as velocidades sônicas compressionais e cisalhantes medidas em poços desviados podem ser altamente afetadas pela anisotropia do tipo VTI, geralmente exigindo correções para este efeito. A modelagem anisotrópica e inversão feita nos perfis sônicos sintéticos mostraram a magnitude do efeito e que ele pode ser corrigido de forma eficiente pelo método proposto. Finalmente, uso uma abordagem de inversão multidimensional não linear para calibrar os modelos propostos e aplicá-los no contexto geomecânico 1D de predição da pressão de poros num reservatório cretácico areno-argiloso e saturado com óleo. Os resultados mostraram uma boa concordância com os dados diretos de pressão de poro e as estimativas através do método tradicional de Eaton. A vantagem da abordagem proposta é a sua consistência ao longo de todo o fluxo de trabalho de interpretação petrofísica do poço, especialmente no que diz respeito à inclusão da porosidade, volume de argila e saturação.

Palavras-chave: Pressão de poro, Eaton, Geomecânica, Geopressões, inversão não linear.

LIST OF FIGURES

LIST OF TABLES

1. INTRODUCTION

The knowledge of abnormal pore pressure is an essential requirement for optimal field development and well design decisions, impacting safety during drilling operations. Pore pressure estimation has a significant value for the oil industry since it helps drilling and oil recovery optimization. Estimates are performed using seismic velocity and sonic log data, following a generic workflow consisting of two main steps: 1) obtaining the compressional velocity (*Vp*) of the formation using available information from seismic and sonic-log data (Sayers et al., 2002; Dutta, 2002; Kan and Swan, 2001; Malinverno et al., 2004); 2) applying a pore pressure transformation that takes velocities into pore pressure with quality control checks to adjust ideal input variables and parameters.

In particular, in young sedimentary basins from Pleistocene to Paleocene, the phenomenon of compaction disequilibrium (or undercompaction) is most responsible for an abnormal increase in pore fluid pressure, also having cases where fluid movements and aquathermal expansion of aquifers also contributes (e.g., Dickinson, 1953). Below tertiary until old Cambrian basins (e.g., Sichuan, China; Timan-Pechora, Russia; and Chaco, Bolivia) with hydrocarbons in a gaseous phase, high overpressures can be related to both undercompaction and unloading mechanisms like fluid expansion.

The pore pressure transformation is done through semi-empirical relations based on effective stress methods developed for non-reservoir rocks (shaly formations), as presented by Hottman and Johnson (1965), Eaton (1975), and Bowers (1995). Very often, such relations have been indiscriminately applied for all formation types, including reservoir sands. It was not until a decade later that authors, led by Carcione et al. (2003), Dvorkin et al. (2002), Sayers et al. (2003), and Doyen et al. (2004), proposed new models for pore pressure estimation in reservoir rocks connecting pore pressure modeling with other petrophysical properties such as porosity and clay volume, what represents an advance for the pore pressure studies. Despite that, the traditional methods are still widely used for shaly rocks and reservoir intervals. In a few words, a simple relation between *Vp* and pore pressure (actually, *Vp* vs. effective pressure, for a given lithostatic pressure) is locally calibrated using pore pressure measurements to yield proper pore pressure estimates over the target intervals. As the elastic properties in sand-shale rocks may vary significantly with porosity and lithology, as has been widely demonstrated in many studies, such as those by Castagna et al. (1985), Han et al. (1986), and Eberhart-Phillips et al. (1989), the estimated pore pressure becomes subject to this potential source of error. Another critical effect not generally considered is due to the pore fluid. Fluid content (water, oil or gas) significantly affects P-wave velocity in reservoir rocks. This effect is more frequently modeled using Gassman equations (Mavko et al., 1998) that separate the bulk modulus contributions of the dry rock frame (porosity and lithology) from that of the pore fluid mixture.

Because of that, in the first part of the work, I present a parametric analysis of P and S-wave velocity models using synthetic laboratory ultrasonic measurements of seismic velocities. Compressional velocity is modeled as a function of differential pressures (effective stress), porosity, shale content, and fluid saturations. This is in line with the idea that a complete approach to pore pressure estimation involves testing new models with all relevant petrophysical parameters and perhaps bringing other seismic attributes to reduce the uncertainty. Here we follow on this path by proposing and testing extended forms of Bowers (1995) and Doyen et al. (2004) formulae, representing pore pressure as a function of compressional velocity, effective stress, porosity, clay, and fluid volumes, as well as pore pressure as a function of shear velocity, effective stress, porosity, and clay.

A problem for pore pressure prediction from sonic velocity data in deviated wells through shally formations is the effect of anisotropy, which requires a preliminary step of sonic logs correction. As directional drilling is standard practice for production optimization during field development, I propose a nonlinear inversion method for compensating this effect in compressional and shear velocities in the second part of this thesis. The anisotropy correction algorithm is developed and validated using a separate proprietary data set. A synthetic data example shows how the methodology works. The inversion anisotropy method proposed following Hornby et al. (2003) shows consistent results in our implementations. Other authors working on this problem in past years are not explicit in exposing technical details of their sonic data correction method.

Finally, to validate our pore pressure study, we make comparative estimations using the Eaton method in the context of a 1D geomechanics modeling that considers estimations only in shales with extrapolation and calibration in sands of an upper cretaceous overpressured shaly sand oil reservoir. The proposed velocity equations for pore pressure estimation follow a nonlinear multidimensional inversion approach to calibrate the proposed models and apply them in the context of a 1D geomechanics pore pressure prediction. Results showed good concordance with the Eaton method and direct pore pressure measures confirming this approach as an alternative way for integrated well-log interpretation applications and pore pressure estimation workflow.

One problem faced in this research was finding an adequate nonproprietary data set to test the methodology. This problem has impacted the way the thesis is organized. After the Introduction (Chapter 1), I present three developments on rock sample and well log scales to validate each solution stage using independent data sets. Chapter 2 presents a rock physics sensitivity analysis using synthetic data and variations in pore pressure, lithology (porosity and clay volume), and saturation. Chapter 3 presents the development of a methodology to correct sonic logs in deviated wells in layered anisotropic formations, which is an essential part of a more general pore pressure prediction workflow. For this development based on anisotropy analysis, I use another synthetic model based on an actual case study. Chapter 4 presents the integrated rock physics and geomechanical approach to pore pressure estimation using synthetic data based on a real case study. Finally, chapter 5 concludes the thesis by synthesizing the main findings and recommendations.

2. ROCK PHYSICS AND PORE PRESSURE SENSIBILITY MODELS

One problem in pore pressure quantification with effective stress methods is that it works more accurately in shale formations due to its compaction behavior (unambiguously, we cannot apply direct pore pressures measures in this kind of rock). In sand or shaly sand formations, effective stress methods are more problematic, considering that compaction is significantly smaller and compressional velocity is strongly affected by porosity, shale content, and fluid saturation. Despite the recent advances in seismic, sonic, and geomechanics domains, the traditional compressional velocity methods are still widely used for shaly rocks and reservoir intervals. On the other hand, conventional geomechanical methods are based on a simple relation between V_P and pore pressure (actually, V_P vs. effective pressure, for a given lithostatic pressure), which is locally calibrated to yield proper pore pressure estimates in the target intervals. The elastic properties in shaly sand rocks may vary significantly with porosity and lithology, as has been widely demonstrated in the rock physics studies, such as those by Castagna et al. (1985), Han et al. (1986), and Eberhart-Phillips et al. (1989), where the estimated pore pressure becomes subject to this potential source of error. Substitution fluid analysis through Gassman equations (Mavko et al., 1998) as a branch of rock physics applications shows that compressional velocity is sensitive to differential pressures, porosity, shale content and fluid saturations as expected. Therefore, a more complete approach to pore pressure estimation involves testing new models with an increased number of petrophysical parameters and perhaps bringing other seismic attributes to reduce the uncertainty.

2.1. Study of Eberhart-Phillips and Doyen velocity models

In this section, I define a rock physic approach to obtain K_{dry} and μ_{dry} (inputs for posterior fluid substitution steps and velocity sensitivity analysis) using empirical differential pressure equations for saturated and consolidated rocks from Eberhart-

Phillips et al. (1989) and Doyen et al. (2004) but conditioned (calibrated) in our survey with dry rocks samples (Holzberg, 2005).

Fluid substitution procedures used in this study for sensitivity analysis of velocities help understand how seismic attributes respond to the rock's fluid content, which is essential for hydrocarbon exploration and reservoir characterization. The goal is to model seismic velocity signatures and responses as a function of lithology, porosity, and fluid variations. Gassmann´s equation (see, e.g., Smith et al., 2003) represents a standard model for fluid substitution analysis, carrying the following principal assumptions: 1) the rock is homogeneous and isotropic, composed by a single mineral and fluid filling the pores; 2) all pores are interconnected (i.e., effective porosity), 3) low-frequency wave propagation regime implying that pore-fluid pressure perturbation can relax instantly during wave passing. Gassmann equation represents the low-frequency end of Biot theory of wave propagation saturated porous medium that describes seismic velocities over a whole range of frequencies (Mavko et al., 1998; Wang, 2001 and Smith et al., 2003).

Fluid properties can be used directly to calculate the elastic stiffness tensor of the rock-fluid system, as in Brown and Korringa's (1975) equations. Fluids affect the compressional-wave velocity, V_P, of the rock-fluid system through density ρ, bulk modulus K and perhaps shear modulus μ (e.g., for high frequency or viscous fluids that support shear stresses), according to the elastic velocity formula

$$V_P = \sqrt{\frac{K+(4/3)\mu}{\rho}} \ . \tag{1}$$

As stated previously, in general terms, Gassmann's theory is based on isotress conditions for an isotropic, homogeneous, monomineralic rock at the low-frequency limit. A common form is

$$K_{sat} = K_{dry} + \frac{\left[1 - \frac{K_{dry}}{K_g}\right]^2}{\frac{\Phi}{K_{fl}} + \frac{(1-\Phi)}{K_g} - \frac{K_{dry}}{K_g^2}}, \tag{2}$$

and

$$\mu_{sat} = \mu_{dry}, \tag{3}$$

where K_{sat} and μ_{sat} are saturated rock bulk and shear modulus respectively to be used in Equation 1 for rock-fluid velocity computation, K_{dry} is "dry" rock bulk modulus, K_g is the grain mineral modulus, Φ is porosity, K_{fl} is the fluid bulk modulus, and μ_{dry} is "dry" rock shear modulus. "Dry" means room dry. According to Gassmann's theory, fluid does not affect shear modulus μ, and has a minor influence on shear-wave elastic velocity V_s, through the density

$$V_S = \sqrt{\frac{\mu}{\rho}} \ , \tag{4}$$

For pore pressure and sensitivity studies based on compressional and shear velocities with differential pressures, Gassmann's equation can be used with different other models to characterize the K_{dry}, K_g, K_{fl} and μ_{dry}. K_g can be computed using the Hashim-Shtrikman's lower limit (Mavko et al, 1998), considering the rock grain as a homogeneous mixture between sand and clay.

Here, I propose a simplified procedure to obtain K_{dry} and μ_{dry} using empirical differential pressure equations for saturated and consolidated rocks from Eberhart-Phillips et al. (1989) and Doyen et al. (2004) after a calibration process with dry rocks samples (Holzberg, 2005). Using these empirical equations calibrated in dry rocks, we get a direct relation between velocities, petrophysical parameters, and pore pressure (differential or effective pressures represent the difference between confining pressure and pore pressure)

$$V_{p(1)} = 5.98 - 8.056\Phi - 1.96\sqrt{C} + 0.638(P_d - e^{-18.38P_d}), \qquad (5)$$

$$V_{s(1)} = 3.73 - 4.79\Phi - 1.61\sqrt{C} + 0.373(P_d - e^{-17.3P_d}), \qquad (6)$$

and

$$V_{p(2)} = 5.84 - 7.5\Phi - 5C + 1(P_d)^{0.4}, \qquad (7)$$

$$V_{s(2)} = 2.1 - 3.1\Phi - 0.7C + 1(P_d)^{0.24}, \qquad (8)$$

where $V_{p(1)}$ and $V_{s(1)}$ in Equation 5 and 6 are calibrated dry rock velocities (in km/s) using the Eberhart-Phillips model, $V_{p(2)}$ and $V_{s(2)}$ in Equation 7 and 8 are the calibrated dry rock velocities (in km/s) using the Doyen model, P_d is differential pressure (in kbar), Φ is porosity and C is the clay content. Both processes of calibrations follow the proposed Han (1962) and Eberhart-Phillips et al. (1989) method called the "forward stepwise multiple regression" in order to obtain the best fitting relationship. It must be highlighted that the coefficients in Equations 5 and 6 are obtained by Holzberg (2005) as part of their doctorate research study using synthetic data measures as a reference of dry consolidated rock. To obtain K_{dry} and μ_{dry} velocity relations using Equations 5-8, it is assumed that elastic modulus in Equation 1 and 4 represent the dry moduli

$$V_{P\_dry} = \sqrt{\frac{K_{dry} + (4/3)\mu_{dry}}{\rho_{dry}}}, \qquad (9)$$

and

$$V_{s\_dry} = \sqrt{\frac{\mu_{dry}}{\rho_{dry}}}, \qquad (10)$$

Rearranging Equation 9 and 10, but using V_p and V_s from Equations 5, 6, 7, and 8 calibrated with dry rocks samples respectively, we obtain for K_{dry} and μ_{dry}, expressions that link these elastic moduli, with porosity, Φ, shale content, C, and differential pressure P_d through the saturated velocities of Eberhart-Phillips and Doyen models, as given by

$$K_{dry} = \rho_{dry}\left\{\left(V_{p(1\ or\ 2)}\right)^2 - {}^4\!/_3\left(V_{s(1\ or\ 2)}\right)^2\right\}, \tag{11}$$

and

$$\mu_{dry} = \rho_{dry}\left(V_{s(1\ or2)}\right)^2, \tag{12}$$

Note that this simplistic procedure of “*drying”* the previous velocity water-saturated rock models for obtaining a K_{dry} relation with petrophysical parameters and differential pressure is a data-driven approximation. Grain density is obtained by a volumetric mean between the densities of each phase

$$\rho_g = \rho_{sand}(1 - C) + \rho_{shale}C, \tag{13}$$

where C is the clay content. The moduli and densities of sand and clay are considered known. For K_{fl} we used the equations presented in Batzle and Wang (1992), where fluids saturations are assumed as homogeneous mixtures of brine and oil. In this formulation, velocities and densities of each mixture phase are modeled by a function of pore pressure, temperature and chemical properties. Wood’s average is also employed to obtain the mixture’s bulk modulus, and the volumetric mean is used to obtain the density (Batzle and Wang, 1992). Since the dry rock models refer to differential pressure, P_d, and the fluid models refer to formation pore pressure, the Terzaghi (1943) relation is introduced in order to uniform the models

$$P_d = P_c - P_p, \tag{14}$$

where P_c is confining pressure, considered to be the same as the overburden pressure and P_p is the formation pressure. The saturated rock density is computed as a volumetric average of solid and fluid phases, given by

$$\rho_{sat} = \rho_g(1 - \Phi) + \rho_{fl}\Phi, \tag{15}$$

where Φ is the porosity, ρ_g is the grain density and ρ_{fl} the fluid density. Gassmann Equation 2 was employed to get saturated bulk rock moduli. Finally, elastic medium wave propagation Equation 1 and 4 were applied to calculate the saturated compressional and shear rock velocities using saturated rock density from Equation 15.

2.1.1. Sensitivity analysis

Following a fluid substitution procedure as well as the rock physic approach to obtain K_{dry} and μ_{dry} using the Eberhart-Phillips et al. (1989) and Doyen et al. (2004) calibrated models with dry rocks samples (Holzberg, 2005) described previously, I apply sensitivity and parametrical analyses employing the parameters and their respective average values listed in Table 6.

Parameter	Average value
C	0.30
ϕ	0.20
S_{oil}	0.5
API(°)	35
T(°C)	40
$S_{cs}(ppm)$	2500
$Pc(MPa)$	23

Table 1: Input parameters for sensitivity analysis between compressional, shear velocities and differential pressures, following the fluid substitution procedure defined in this work where C is the clay content, ϕ the porosity, *Soil* the oil saturation, API(°) is the gravity of crude oil, T(°C) is the temperature, $Scs(ppm)$ is the water salinity and $Pc(MPa)$ is the confining pressure.

The confining pressure P_c representing the overburden in this work is fixed to evaluate the pore pressure variations. Mineral properties for sand and clay used in this analysis are taken from Goldberg & Gurevich (1998): $K_{sand} = 39\ GPa$, $K_{clay} = 20\ GPa$, $\mu_{sand} = 33\ GPa$, $\mu_{clay} = 7.6\ GPa$ and $\rho_{sand} = \rho_{clay} = 2.65\ g/cm^3$.

Figure 1 shows the drained modeled Vp vs Pd and Vs vs Pd with the previously defined procedure to obtain the dry moduli in a consolidated formation, using Doyen and Eberhart-Phillips relations (Eq. 5-8 calibrated with synthetic rock dry samples).

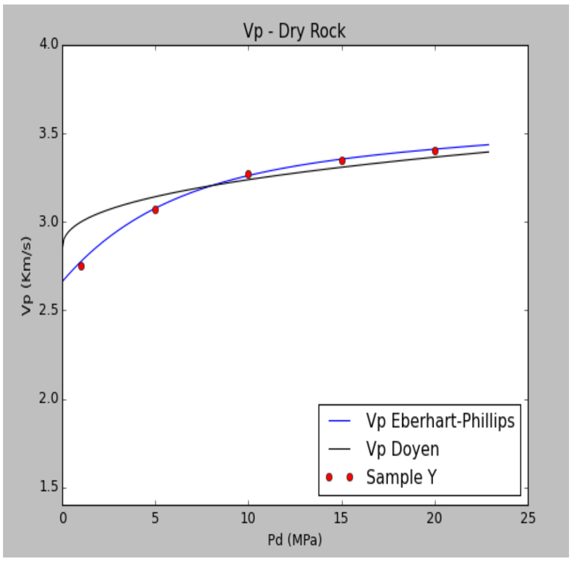

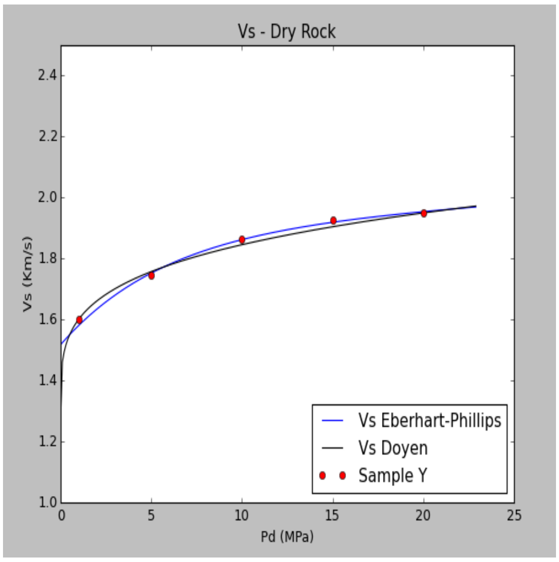

Figure 1: Vp *vs.* Pd and Vs *vs* Pd dry rock relations following the previously defined procedure to obtain the dry moduli in a consolidated formation, using Doyen (Black curve) and Eberhart-Phillips relations (blue curve) with Equations 5-8 calibrated with synthetic rock dry samples (Sample Y). The Sample Y red dots are the synthetic data simulating dry sand shale rocks with porosity and clay content of 0.20 and 0.3, respectively (Holzberg, 2005).

The synthetic data is displayed in Figure 1 (red dots): the Eberhart-Phillips model is fitted to obtain their respective coefficients (Eq. 5 and 6), corresponding to a consolidated dry rock reference data (Holzberg, 2005) with porosity and shale content of 0.3 and 0.2 respectively to compare the fitted results with the dry rock calibrated Doyen model (Eq. 7 and 8). Figure 2 shows Vp *vs.* Pd and Vs *vs* Pd relations after a fluid substitution following the previously defined procedure using the respective dry rock calibrated models (Doyen and Eberhart-Phillips relations).

Figure 3 shows a porosity influence in Vp vs. Pd and Vs vs. Pd following the fluid substitution procedure defined previously in a consolidated formation, coupled in the Gassmann model through Equation 2. The extensions E and D shown in the textbox of Figures 3, 4, and 5 refer to Eberhart-Pillips and Doyen model curves, respectively. The porosity during this sensitivity analysis varied from 0.1 to 0.3, while the other parameters are fixed.

As expected in consolidated rocks, the compressional velocity (Vp) is highly sensitive to porosity, with velocity decreasing with increasing porosities in both models. The shear velocity (Vs) also shows high porosity sensitivity in both models but with the Doyen model being slightly less sensitive.

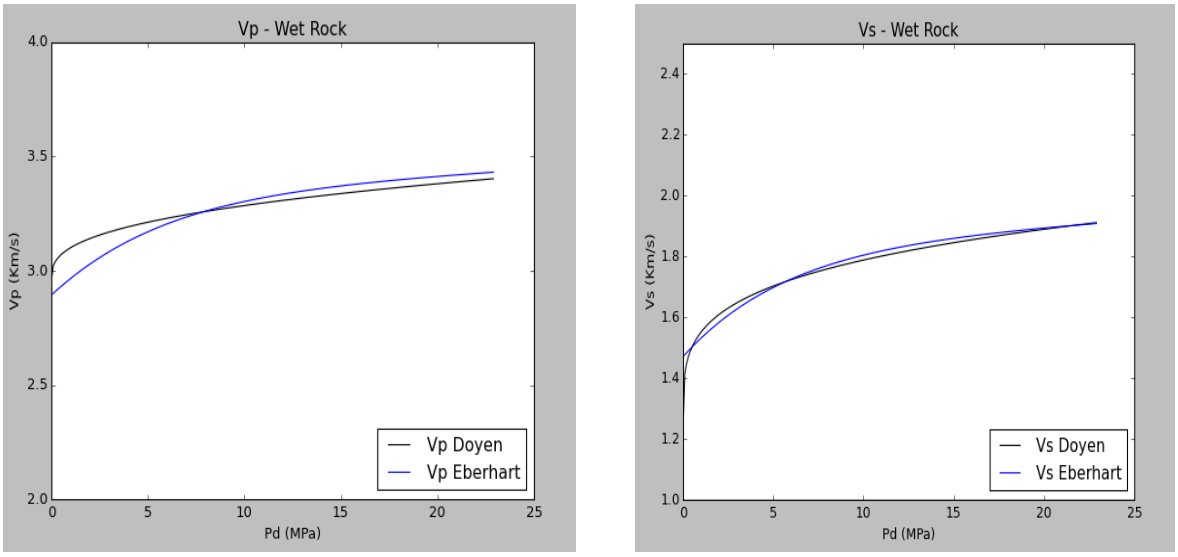

Figure 2: Vp *vs.* Pd and Vs *vs* Pd relations after a fluid substitution following the previously defined procedure using dry rock calibrated Doyen and Eberhart-Phillips relations (Eq. 5-8).

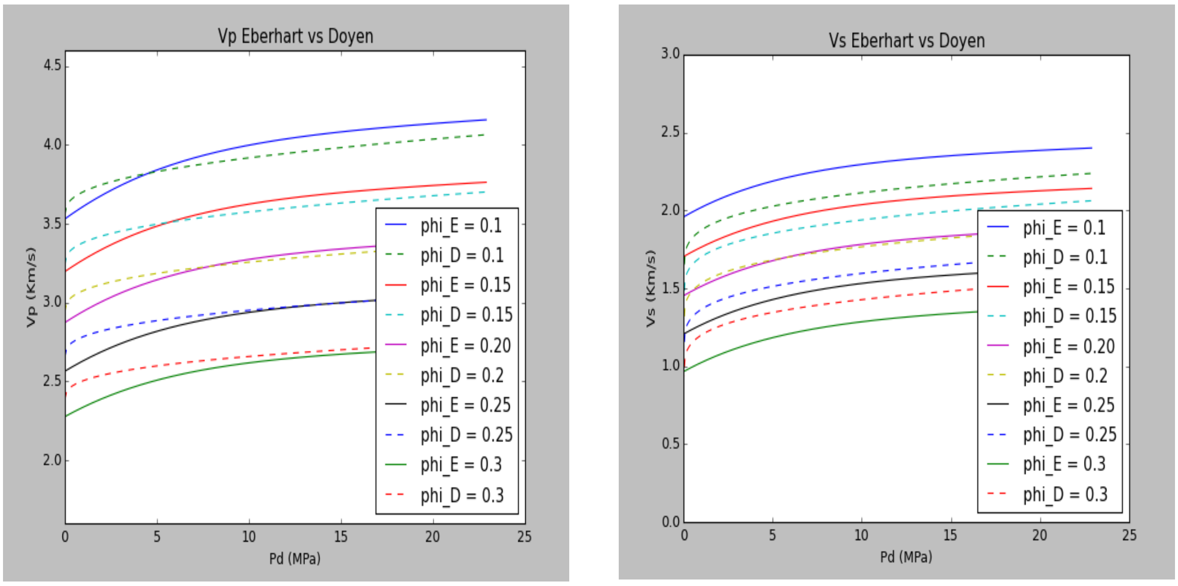

Figure 3: Porosity influence in Vp vs. Pd and Vs vs. Pd following the previously defined fluid substitution procedure and using Doyen and Eberhart-Phillips calibrated dry rock relations (Eq. 5-8).

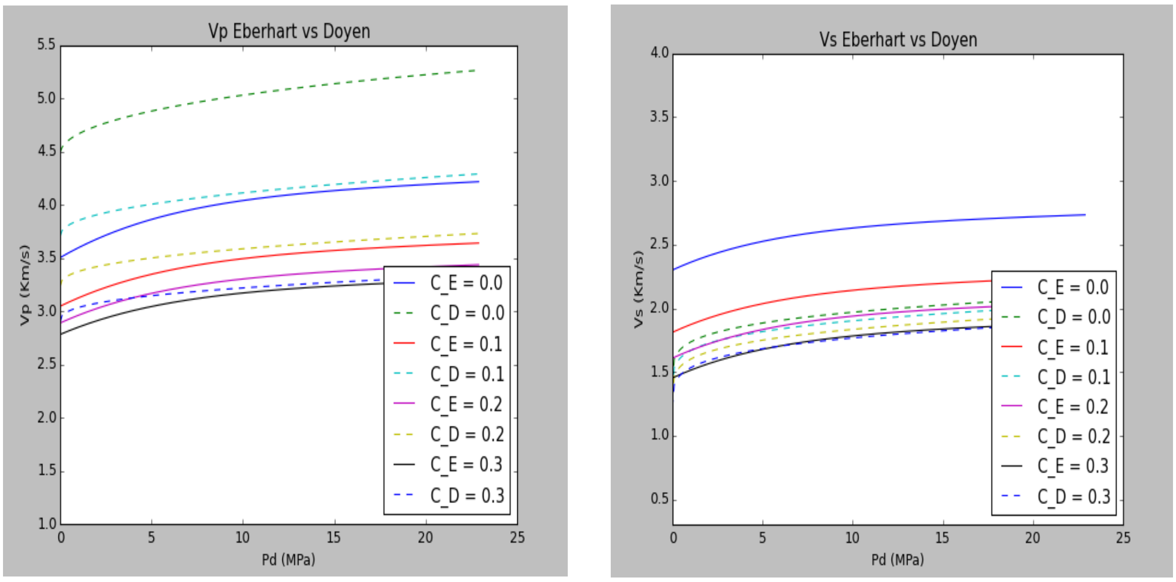

Figure 4: Clay content influences Vp vs. Pd and Vs vs. Pd relations following the previously defined fluid substitution procedure and using Doyen and Eberhart-Phillips calibrated dry rock relations (Eq. 5-8).

Figure 4 shows the clay content influence in Vp vs. Pd and Vs vs. Pd following the fluid substitution procedure defined previously. Similarly, with the porosity effect, the clay content also tends to reduce velocities when increased but with less impact in comparison with porosity, as observed in Figures 3 and 4 for both models. Vs also shows clay content sensitivity in both models but with a lower degree on the Doyen model. Interestingly, compressional velocity variations with clay content are more significant when the clay content increases from 0 to 10 % and from 10 to 20 %, agreeing with Han et al. (1986) observations.

For the porosity and clay content sensitivity, the rock was saturated with a homogeneous brine and dead oil mixture with the same proportion. Figure 5 shows the dead oil saturation influence in Vp vs. Pd and Vs vs. Pd following a fluid substitution procedure in a consolidated formation, increasing saturation from 0 to 70%. API Gravity oil used in this sensitivity test is 35°. As expected, increasing oil saturation does not affect shear velocities and reduces the compressional velocities, but with less impact than porosity and clay content effects. Increasing variations of API also tend to have an analogous behavior when increasing oil saturations (Holzberg, 2005).

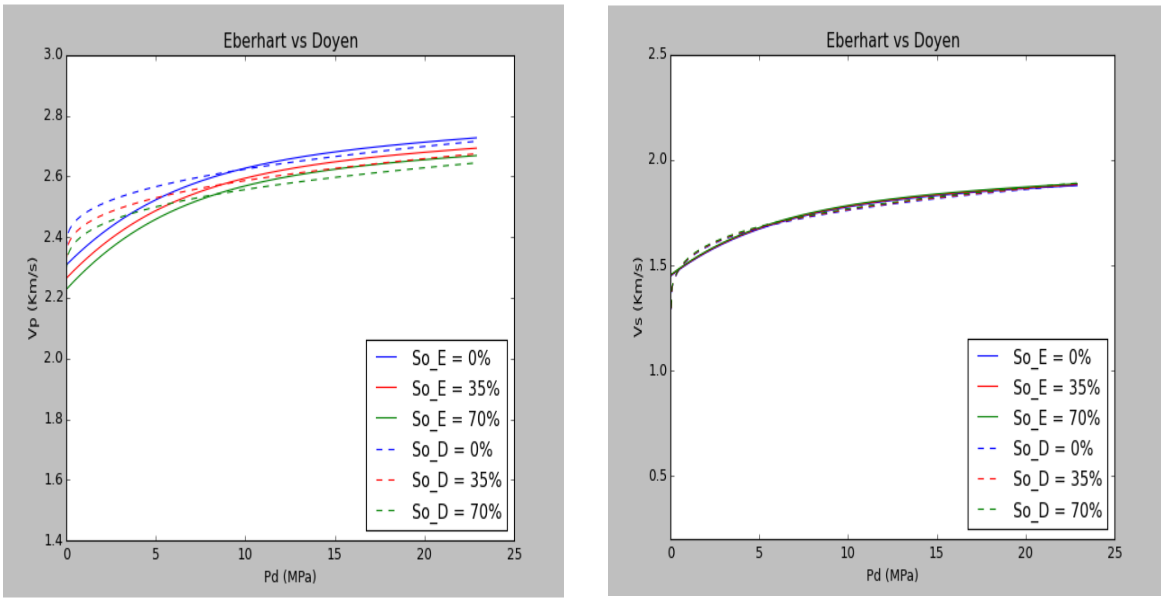

Figure 5: Oil saturation influences Vp vs. Pd and Vs vs. Pd relations following the previously defined fluid substitution procedure and using Doyen and Eberhart-Phillips calibrated dry rock relations (Eq.5-8).

2.2. Pore pressure proposed equations

Taking into account the previous analysis of fluid substitution for compressional and shear velocity sensitivity responses in the function of differential pressure, porosity, clay content, and oil saturation and following Sayers et al. (2003) as well as Doyen et al. (2004), I start from an extended empirical expression of P-wave velocity as a function of pore pressure, P_P, overburden pressure, P_o, porosity, $\emptyset$, clay volume, C, adding the variable oil volume V_{oil}:

$$V_P = a_1 - a_2\emptyset - a_3C - a_4V_{oil} + a_5(P_o - P_P)^{a_6}, \qquad (16)$$

and an empirical analog Doyen expression of S-wave velocity as a function of pore pressure P_P, overburden pressure P_o, porosity $\emptyset$, and clay volume C:

$$V_S = b_1 - b_2\emptyset - b_3C + b_4(P_o - P_P)^{b_5}, \qquad (17)$$

where $\boldsymbol{a_i},\ \boldsymbol{i} = \mathbf{1}, \dots, \mathbf{6}$ and $\boldsymbol{b_i},\ \boldsymbol{i} = \mathbf{1}, \dots, \mathbf{5}$ are the model coefficients, whose values are determined by calibration using well-log data. In the above equations, the velocity dependence on differential (or effective) pressure, given by the $\boldsymbol{P_o} - \boldsymbol{P_P}$, is equivalent to that proposed by Bowers (1995), with the terms $\boldsymbol{a_1} - \boldsymbol{a_2}\emptyset - \boldsymbol{a_3C} - \boldsymbol{a_4V_{oil}}$ in Equation 16, compactly represented by a constant value called the zero-stress mudline velocity, $\boldsymbol{V_o}$, in his model (Bowers method was only based on compressional velocity). In analogy with Bowers, $\boldsymbol{b_1} - \boldsymbol{b_2}\emptyset - \boldsymbol{b_3C}$ term in Equation 17 would also represent the constant value called the zero-stress mudline velocity, $\boldsymbol{V_o}$. By introducing these terms in our model, we can account for variations in porosity, lithology, and volume of oil when using the first expression in compressional velocities and account for variations in porosity and lithology when using the second expression in the function of shear velocities. These developments are also related to models presented by Han et al. (1986) and Eberhart-Phillips et al. (1989) in terms of lithology effects studies. Taking Equation 16 and 17, we can rewrite it to obtain expressions for the pore pressure transformation, given by:

$$P_P = P_o - \left[\frac{1}{a_5}\left(V_p - a_1 + a_2\emptyset + a_3C + a_4V_{oil}\right)\right]^{\frac{1}{a_6}}, \qquad (18)$$

and

$$P_P = P_o - \left[\frac{1}{b_4}(V_s - b_1 + b_2\emptyset + b_3C)\right]^{\frac{1}{b_5}}, \qquad (19)$$

Equations 18 and 19 may be applied point-by-point in a 3-D MEM or 1-D MEM, assuming that a velocity is available from seismic inversion or interpolated using data from nearby wells, including sonic logs, porosity, shale volume and fluid volumes. Fluids do not influence the S-wave formulation. The overburden pressure, $\boldsymbol{P_o}$ required in the calculation of $\boldsymbol{P_P}$ can be obtained by integration of the density function, given by

$$P_o(z) = g\int_0^z \rho(z)dz, \qquad (20)$$

where Z is the vertical depth, g is the acceleration of gravity and ρ is the bulk density. In practice, the integral is calculated from a density cube either from elastic inversion or well-log data from the surface to depth Z , as commonly done during 1-D MEM building.

3. ANISOTROPY THEORY AND CONSIDERATIONS

Sound waves travel through some rocks with different velocities in different directions. This phenomenon, called elastic anisotropy, occurs if there is a spatial ordering of crystals, grains, cracks, bedding planes, joints, or fractures. This alignment causes waves to propagate fastest in the stiffest direction (Armstrong et al., 1994). It is well known, for example, that shales exhibit anisotropic behavior. Failure to account for anisotropy can lead to errors in seismic domain procedures such as normal-moveout correction, dip-moveout correction, migration, and amplitude-versus-offset (AVO) analysis. Moreover, in the geomechanical domain, errors due to anisotropy can be critical in procedures for pore pressure, mechanical rock properties, and situ stress predictions that are essential input data for wellbore stability design in order to get a trustable construction of failure and tensile models (predicting the pore collapse and initiation-propagation of hydraulic fractures).

Considering the problem related to the VTI (transversely isotropic with a vertical axis of symmetry) anisotropy phenomenon affecting sonic data in deviated wells, it is necessary to develop a robust method for measuring and modeling acoustic anisotropy to compensate for this effect on the velocity measurements. Furthermore, pore pressure and mechanical rock properties estimation from well-logs relies mainly on sonic data, which can be significantly affected. Although the pore pressure data example presented in the next chapter comes from a vertical well (not affected by VTI anisotropy), a more general application requires dealing with deviated wells widely used in reservoir development. The anisotropy inversion survey done through the synthetic sonic log data shows how the borehole sonic velocities can be affected and efficiently corrected by the proposed method.

3.1. Types of anisotropy

In general terms, there are two idealized alignment styles in earth materials - horizontal and vertical – giving rise to two basic types of anisotropy (Fig. 6). These two oversimplified but convenient models describe how elastic properties, such as velocity or stiffness, can vary in these types of symmetries (Armstrong et al., 1994). In the simplest horizontal or layered case, elastic properties may vary vertically, such as from layer to layer, but not horizontally. Such a material is called transversely isotropic with a vertical axis of symmetry (VTI). Waves generally travel faster horizontally, along with layers, than vertically. Detecting and quantifying this type of anisotropy is important for correlation purposes, such as comparing sonic logs in vertical and deviated wells and for borehole and surface seismic imaging and studies of amplitude variation with offset (AVO).

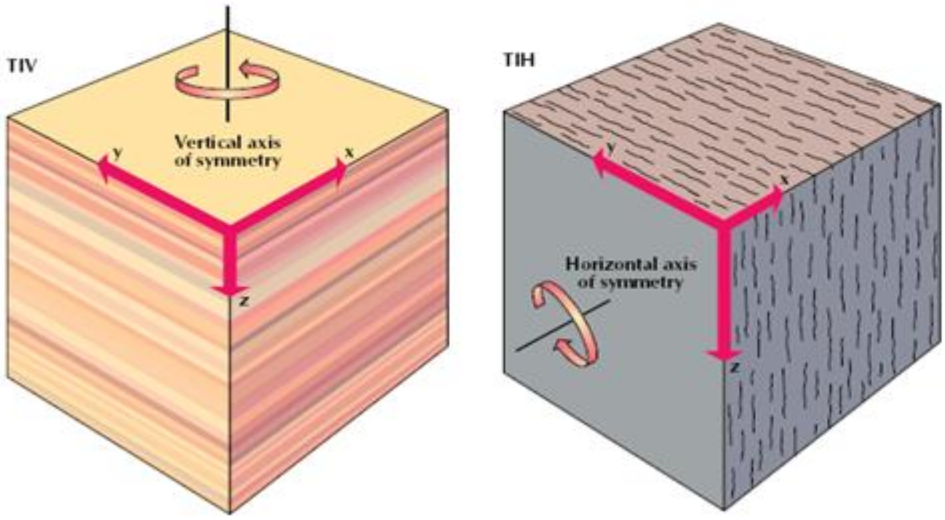

Figure 6: Simple geometries for elastic anisotropy characterization. VTI (left) and HTI (right) symmetry axis models are commonly used for conventional material alignments and velocity characterization with their respective planes of polarization. Armstrong et al. (1994).

The simplest case of the second type of anisotropy corresponds to a material with aligned vertical weaknesses such as cracks or fractures or unequal horizontal stresses, as seen on the right side of Figure 6. Elastic properties vary in the direction crossing the fractures but not along the plane of the fracture. Such a material is called transversely isotropic with a horizontal axis of symmetry (HTI). Seismic waves traveling along the fracture generally travel faster than waves crossing the fractures. Identifying and characterizing this type of anisotropy using elastic theory principles is vital to get appropriate information about rock elastic and mechanical properties, stress, and fracture density with orientation. These parameters are essential for designing hydraulic fracture jobs and for understanding horizontal and vertical permeability anisotropy. Another kind of earth material alignments can also be described by more complex models like TTI, orthorhombic, and tilted symmetries.

Identifying types of anisotropy requires understanding how waves can travel in polarization terms (see Fig. 7). Waves come in three styles of polarization, all of which involve tiny motion of particles relative to the undisturbed material. In isotropic media, compressional waves have particle motion parallel to the direction of wave propagation, and two shear waves have particle motion in planes perpendicular to the direction of wave propagation.

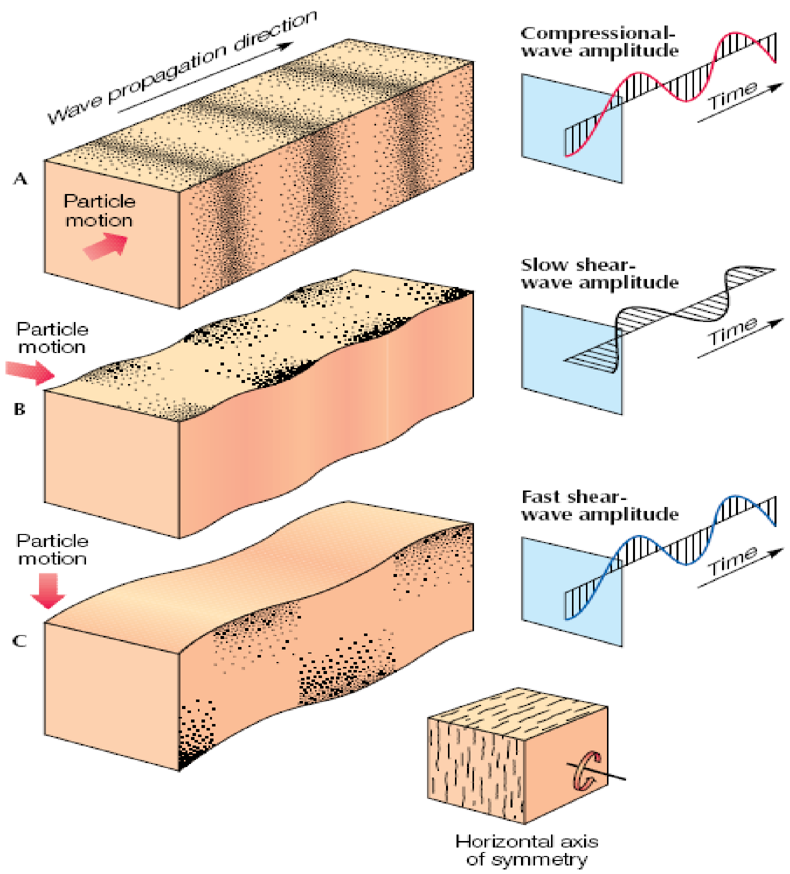

Figure 7: Compressional and shear waves. Armstrong et al. (1994).

In an anisotropic material, waves travel faster when their particle motion is aligned with the material's stiff direction. For P-waves, the particle motion and propagation direction are nearly the same. When S-waves travel in a given direction in an anisotropic medium, their particle motion becomes polarized in the material's stiff (or fast) and compliant (or slow) directions. According to their respective velocity, the waves with differently polarized motions arrive at their destination at different times. This phenomenon is called shear-wave splitting, or shear-wave birefringence - a term, like anisotropy, with origins in optics. Splitting occurs when shear waves travel horizontally through a layered (VTI) medium or vertically through a fractured (HTI) medium.

3.2 Hooke's law

An elastic material deforms under external forces (stress) but returns to its original shape when the stress is removed. For small deformations, the stress is roughly proportional to the strain in many solids. Young's modulus (E), a measure of stiffness, is a proportionality constant used to relate stress and strain. This linear relationship between stress and strain is Hooke's law, which is the basis for linear elasticity theory (Nayfe,1995).

Anisotropy models for seismic and geomechanics work in elastic media can be constructed through the generalized Hooke's law,

$$\sigma_{ij} = c_{ijkl}\varepsilon_{kl}, \tag{21}$$

which shows that the second-order stress tensor σ_{ij} is equal to the second-order strain tensor ε_{kl}, multiplied by the symmetric fourth-order stiffness tensor c_{ijkl}, also called elasticity tensor (Nayfe,1995).

The generalized Hooke's equation can be described in a matrix with sixth components, as observed in Figure 8. The matrix on the left shows normal and shear stresses; the one in the center expresses stiffness parameters modeled for a VTI medium, and the matrix on the right shows normal and shear strains.

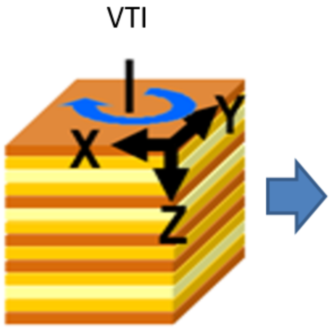

$$\sigma_{ij} = C_{ijkl}\varepsilon_{kl} - \alpha_{ij}P_p$$

$$\begin{bmatrix} \sigma_{xx} \\ \sigma_{yy} \\ \sigma_{zz} \\ \tau_{xz} \\ \tau_{yz} \\ \tau_{xy} \end{bmatrix} = \begin{bmatrix} C_{11} & C_{12} & C_{13} & 0 & 0 & 0 \\ C_{12} & C_{22} & C_{23} & 0 & 0 & 0 \\ C_{13} & C_{23} & C_{33} & 0 & 0 & 0 \\ 0 & 0 & 0 & C_{44} & 0 & 0 \\ 0 & 0 & 0 & 0 & C_{55} & 0 \\ 0 & 0 & 0 & 0 & 0 & C_{66} \end{bmatrix} \begin{bmatrix} \varepsilon_{xx} \\ \varepsilon_{yy} \\ \varepsilon_{zz} \\ \gamma_{xz} \\ \gamma_{yz} \\ \gamma_{xy} \end{bmatrix}$$

$$\sigma_{xx} = C_{11}\varepsilon_{xx} + C_{12}\varepsilon_{yy} + C_{13}\varepsilon_{zz}$$
$$\sigma_{yy} = C_{12}\varepsilon_{xx} + C_{22}\varepsilon_{yy} + C_{23}\varepsilon_{zz}$$

Figure 8: Generalized Hooke’s law applied in a VTI medium – Stress vs. Strain.

3.3. TIV or VTI model

Understanding seismic wave propagation through overlying strata determines successful imaging of subsurface features in the earth (Hornby et al., 2003). Shales makeup 75 % of most sedimentary basins and overlie most hydrocarbon-bearing reservoirs. In general, the elastic properties of shale are known to be anisotropic (Jones and Wang, 1981; Banik, 1984; Tosaya and Nur, 1989; White et al., 1989; Miller and Chapman, 1991, Hornby, 1995, 1998). The actual anisotropy of shales depends on their porosity, burial history, and other intrinsic factors like organic content. Modeling dynamic mechanical rock properties in anisotropic materials with vertical transverse isotropy (VTI) requires the characterization of five independent elastic moduli (or stiffness coefficients following Hooke’s law) rather than the two independent moduli for isotropic materials (see, e.g., Walsh et al., 2007). Standard sonic and density logs provide information for computing two of these elastic moduli, while a third moduli may be interpreted using advanced sonic tools. However, there is no method for obtaining all five parameters from well measurements at a single well. The inherent anisotropy of shales must be considered for seismic tasks like structural imaging of subsurface features, more advanced techniques such as amplitude variation with offset (AVO) analysis of hydrocarbon-bearing reservoirs (Wright, 1987), and geomechanics where velocities are an essential parameter for pore pressure and mechanical properties estimation (Hows et al., 2013).

As stated previously, for composites whose overall properties are transversely isotropic (TI), there are five unique elastic constants. The elastic stiffness tensor C for a VTI medium following Hooke's law in Equation 21 can be written using the Voigt (two-index) notation as:

$$C = \begin{pmatrix} C_{11} & C_{12} & C_{13} & 0 & 0 & 0 \\ C_{12} & C_{11} & C_{13} & 0 & 0 & 0 \\ C_{13} & C_{13} & C_{33} & 0 & 0 & 0 \\ 0 & 0 & 0 & C_{44} & 0 & 0 \\ 0 & 0 & 0 & 0 & C_{44} & 0 \\ 0 & 0 & 0 & 0 & 0 & C_{66} \end{pmatrix}, \tag{22}$$

where C_{44} is the out-of-plane shear modulus that is equal to C_{55} for a VTI medium, C_{66} is the in-plane shear modulus, C_{11} is the in-plane compressional modulus, C_{33} is the out-of-plane compressional modulus, $C_{12} = C_{11} - 2C_{66}$, and C_{13} is an important constant that controls the shape of the wave surfaces (Hornby et al., 2003). Four of these parameters can be expressed in terms of measured velocities using the following expressions (Auld, 1990):

$$C_{11} = \rho V^2{}_{PH}, \tag{23}$$

$$C_{33} = \rho V^2{}_{PV}, \tag{24}$$

$$C_{66} = \rho V^2{}_{SH}, \tag{25}$$

and

$$C_{44} = \rho V^2{}_{SV}, \tag{26}$$

where ρ is bulk density and, assuming a vertical axis of symmetry, V_{PH} and V_{SH} are the horizontal P- and S-wave velocities and V_{PV} and V_{SV} are the vertical P- and S-wave velocities. Solutions for C_{13} is more complicated than the previous ones, but for an in-phase plane-wave propagation at 45°, C_{13} can be expressed as

$$C_{13} = 0.5\left[(4\rho V^2{}_{45^\circ} - C_{11} - C_{33} - 2C_{44})^2 - (C_{11} - 2C_{33})^2\right]^{1/2} - C_{44} \,, \qquad (27)$$

where V_{45° is a compressional (qP) measurement taken at an angle of 45° relative to the axis of symmetry. The direction-dependent compressional velocities through the material can be found by using the Christoffel equations (Mavko et al., 1998) and are given by:

$$V_p(\theta) = \left[(C_{11}\sin^2(\theta) + C_{33}\cos^2(\theta) + C_{44} + M(\theta)^{0.5})/2\rho\right]^{1/2}, \qquad (28)$$

where

$$M(\theta) = \left[(C_{11} - C_{55})\sin^2(\theta) - (C_{33} - C_{55})\cos^2(\theta)\right]^2 + (C_{13} + C_{55})^2 \sin^2(2\theta), \qquad (29)$$

where θ is the angle between the axis of symmetry and the wave propagation direction, ρ is mass density, and the C_{ij} are elements of the elastic stiffness matrix described by Equation 23 – 27. Following Thomsen (1986) assumptions, seismic anisotropy in a VTI medium is weak and compressional velocity can be expressed in terms of their deviation from the vertical velocity as follows:

$$V_p(\theta) \approx V_{p0}(1 + \delta \sin^2\theta \cos^2\theta + \varepsilon \sin^4\theta), \qquad (30)$$

where

$$V_{p0} = \sqrt{C_{33}/\rho}, \qquad (31)$$

V_{p0} is the P wave velocity in the direction of the vertical axis of symmetry as described through Equation 24 (polarized in the vertical direction). Considering the VTI mathematical matrix notations and solutions based on Hooke's law, it is convenient for anisotropy analysis to redefine the five elastic coefficients in terms of two elastic moduli (vertical and horizontal young modulus and Poisson ratio, respectively) or three anisotropy parameters. The three non-dimensional anisotropy parameters as defined by Thomsen (1986) are ε, γ, and δ:

$$\varepsilon = \frac{C_{11} - C_{33}}{2C_{33}}, \tag{32}$$

$$\gamma = \frac{C_{66} - C_{44}}{2C_{44}}, \tag{33}$$

$$\delta = \frac{(C_{13} + C_{44})^2 - (C_{33} - C_{44})^2}{2C_{33}(C_{33} - C_{44})}, \tag{34}$$

where ε is the P-wave anisotropy factor for horizontal to vertical compressional polarized velocities, γ is the S-wave anisotropy factor for horizontal to vertical shear polarized velocities, and δ is a critical factor that depends on the shape of the P- and qS-wave polar surfaces (Walsh et al., 2007).

3.4. Sonic tools

Modern sonic tools provide reliable ground data on formation velocities directly used in many different applications, such as seismic imaging and inversion, synthetic seismograms and well-to-seismic ties, and pore pressure, elastic and mechanical parameters estimation. Where anisotropy is present, velocities from deviated wells differ from the expected responses for vertical wells, indicating the angle dependency of sonic measurements (Furre and Brevik, 1998). Hornby et al. (2003) show that shale anisotropy can affect the sonic slowness (inverse of velocity) in the order of ~15% for deviation of 39° to almost ~35% for deviation of 67°. Hence, VTI anisotropy causes the measured velocities in a deviated well to be faster than would be measured in a vertical well due to a change of the polarization wave propagation direction.

Commonly a borehole sonic tool provides a measurement of the qP mode at the angle of the borehole relative to the axis of symmetry. If crossed-dipole shear measurements (Fig. 9) are available, the two shear arrivals correspond to the qSV and SH modes (Alford, 1986, Hornby, 1995).

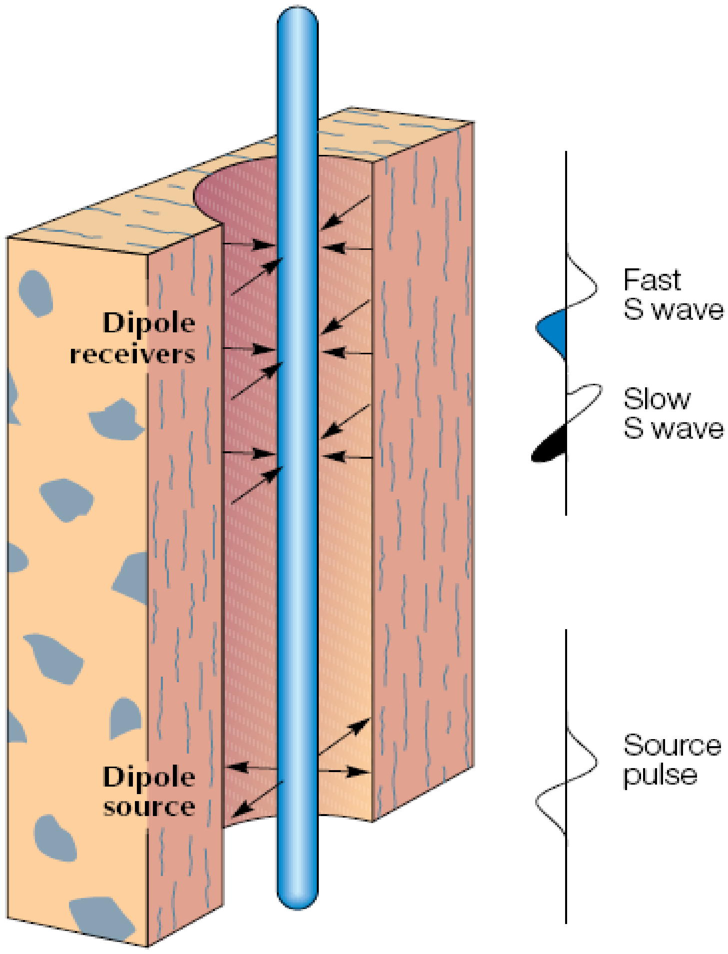

Figure 9: Shear wave splitting in a borehole – Dipole Shear tools (Armstrong et al., 1994).

Advance in sonic tools platforms (Walsh et al., 2007) can provide shear velocities polarized in vertical and horizontal planes, as seen in Figure 10. For compressional velocities in vertical wells, the vertical compressional velocity is always measured (used for C_{33} computation). For horizontal compressional velocities orthogonally polarized (C_{11} and C_{22}), measurements must be done in a horizontal well. Shear velocities can be measured in the horizontal and two vertical planes, as observed in Figure 10 (fast and slow shear velocities computed from cross-dipole data and horizontal Stoneley shear velocity from monopole data), yielding the three shear modulus, C_{44}, C_{55}, and C_{66}.

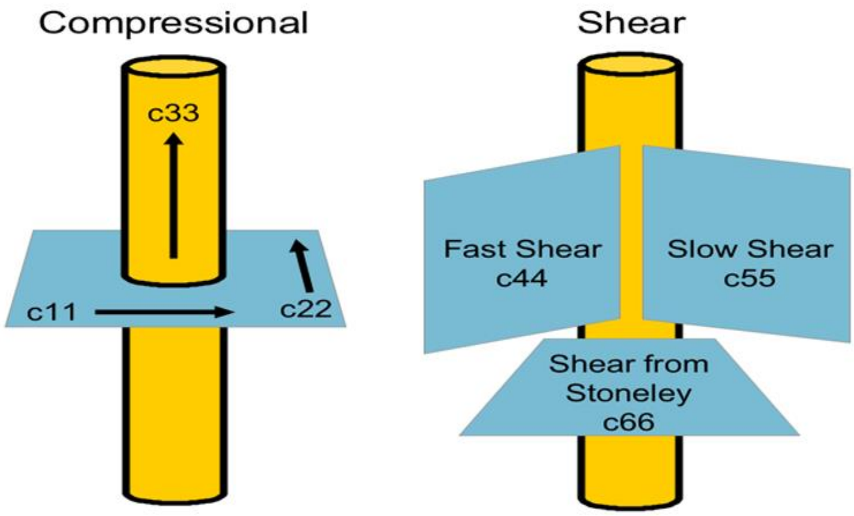

Figure 10: Visualization of compressional and shear slowness polarization planes measured by advanced sonic tools.

3.5 VTI study case

Since the vertical-to-horizontal velocity anisotropy can reach approximately 30% in shales (Hornby et al., 2003), it can be problematic to use sonic logs in deviated wells for pore pressure and mechanical properties estimation in geomechanics and even for synthetic seismogram computation. The inversion done in this study used an iterative non-linear numerical optimization algorithm implemented firstly through an internal set of data to validate the method using two wells penetrating a homogenous shale section at different angles. The inversion scheme used P and S-wave sonic logs at a range of borehole angles (between 35 to 45 degrees) to estimate the five VTI stiffness anisotropy parameters coefficients following Hooke's law and Christoffel equations in order to compute the called Thomsen parameters ε, γ and δ (Thomsen, 1986) and the verticalized P and S-wave velocities. If crossed-dipole shear measurements are available (more reliable for WL tools and point of discussion for LWD tool technologies), the two shear arrivals measure the qSV and SH modes representing the fast and a slow shear after Alford rotation processing (Alford, 1986; Hornby et al., 1995). After validating this algorithm, I created synthetic data for additional testing purposes with a simulated well deviation reaching a maximum of approximately 42°. The synthetic data is analyzed and presented in the next section, considering only compressional data and anisotropy effects in the P-wave during the inversion.

The inversion algorithm implemented through a Python language platform is formulated as an unconstrained non-linear problem, using the quasi-Newton optimization method with the Broyden–Fletcher–Goldfarb–Shanno (BFGS) algorithm that is also a popular algorithm for parameter estimation in machine learning (Fletcher & Roger, 1987; Mascarenhas W. F., 2004). It must be highlighted that during the last years, several publications about sonic verticalization and correction procedures (VTI anisotropy compensation effects), were not so straightforward in terms of specific workflow steps and technical approaches (state of the art) for sonic anisotropy correction.

3.5.1. Synthetic model

A two-well synthetic model with three thick homogenous layers is proposed for this study, considering average gamma-ray values for shales and clean sands. The compressional slowness defined for this synthetic example was for the middle formation in a range of 80 to 120 us/ft following Brie et al., (2000) classification.

Figure 11 shows the synthetic model where GR is set to 77 API for SH1 (shale layer in the top), 27 API for SAND, and 83 API for SH2 (shale layer in the bottom). Compressional slowness in the first shale layer is set to 114 us/ft for the vertical well (DTCO_MODEL_W1) and was introduced as a VTI anisotropy effect a difference of 10% (104 us/ft) for the Compressional slowness of the deviated well (DTCO_MODEL_W2). Compressional slowness in the sand layer is set with 90 us/ft for both wells (homogenous isotropic section).

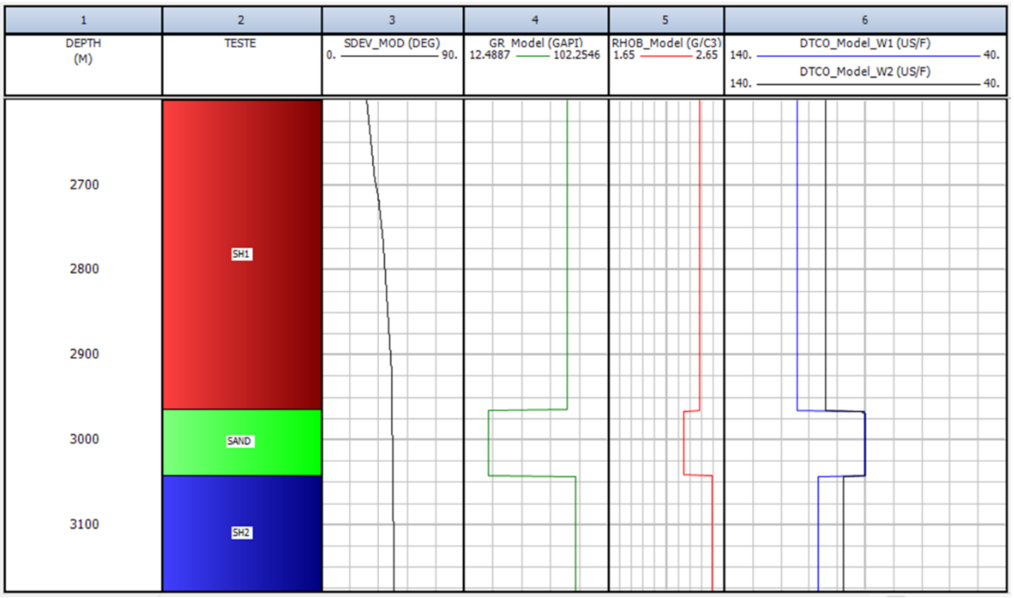

Figure 11: Synthetic model constructed for the inversion study with three thick homogenous layers (two shales and one sand). DTCO_Model_W1 (blue curve in track 6) represents the compressional slowness of the vertical well, and DTCO_Model_W2 (black curve in track 6) represents the slowness of the deviated well affected by VTI anisotropy. Deviation modeled reaches a maximum of 42° (SDEV_MOD).

For the second shale layer, the compressional slowness is set to 107 us/ft for the vertical well and was introduced as a VTI anisotropy effect, a difference of 10% (97 us/ft) for the compressional slowness of the deviated well, as seen in Figure 11. The density log is computed using the next power empirical relations, listed in Table 2, through compressional slowness of the vertical well for SH1, SAND and SH2 sections.

Sections	Density Relations
SH1	$RHOB=3.284\ DTCO^{-0.06}$
SAND	$RHOB=12.05\ DTCO^{-0.372}$
SH2	$RHOB=4.055\ DTCO^{-0.1}$

Table 2: Density power empirical relations through compressional slowness of the vertical well, for SH1, SAND and SH2 sections.

The final objective is to use the inverted coefficient stiffness to compute the anisotropy parameters ε and δ, using borehole sonic measurements at different angles relative to the axis of symmetry, which can be used to obtain the vertical P-wave velocity (V_{PV}). We assume the shale is transversely isotropic with a vertical axis of symmetry (VTI) and the shale properties do not change significantly from well to well.

3.5.2. Inversion procedure

The approach used in this study minimizes the *rms* error between a modeled P-wave velocity surface and the measured data through a constructed *Python* algorithm that uses the non-linear Broyden-Fletcher-Goldfarb-Shanno (BFGS) numerical optimization method from the *SciPy* optimization library (Lewis & Overton, 2008). The rms error was defined as:

$$\left(\frac{1}{N} \sum_{1}^{N} (V_{PM}(\theta) - V_{PE}(\theta))^2 \right)^{1/2}, \tag{35}$$

where N is the total number of individual signals measured (waveforms acquired by depth), $V_{PM}(\theta)$ is the measured velocity at the well deviation angle θ and $V_{PE}(\theta)$ is the modeled P-wave velocity through Equation 28. Required for the computations is a rough initial estimate of stiffness modulus C_{11}, C_{33}, C_{44} and $V45°$ as well as a vertical velocities V_{PV} / V_{SV} relations using Castagna's mud rock expression (Castagna et al., 1985)

$$V_{SV} = \frac{(V_{PV} - 1.36)}{1.16} \quad , \tag{36}$$

The inversion procedure works as follows. First, make an initial guess for V_{PV} using the vertical well data as a reference. Estimate V_{SV} using a measured value of fast shear velocity if available from a vertical well or using Equation 36 as done in this synthetic case. Second, compute initial values of C_{11}, C_{33}, assuming *1.2x*V_{PV}

and V_{PV}, respectively, using Equations 23 and 24 with an average density from the synthetic curve as initial guess and for C_{44} with the previous V_{SV} through Equation 26. Set $V45°$ to V_{PV} for estimate C_{13} using Equation 27 and M using Equation 29. Third, compute the P-wave velocity surface using stiffness coefficients C_{11}, C_{33}, C_{44}, and the parameter M through Equation 28. Then minimize the *rms* error interactively with Equation 35 between the measured velocities and the modeled velocities through the BFGS numerical optimization algorithm with the inversion sequence implemented through Python optimization libraries. After these minimizations, the final C stiffness coefficients obtained during this inversion in the selected shale zone (assumed 100% shale) can be used to estimate the anisotropy parameters ε and δ directly using Equation 32 and 34, respectively.

Optimization terminated successfully.	
CFV	0.002
INTER	8
FE	110
GE	22
RMSE	0.079

Table 3: Optimization diagnostic BFGS python panel (inversion diagnostic results of the minimized function).

Optimization diagnostic results of the algorithm at this example are detailed in Table 3, where CFV is the current function value, INTER is the number of interactions during the inversion, FE is the number of function evaluations, GE is the gradient evaluations and RMSE represent the error minimization reached during the final inversion.

Figure 12 shows a polar plot of the computed P velocities for anisotropic (red curve) using the Thomsen polar Equation 30 with the estimated shale anisotropic coefficients of ε=0.31 and δ=0.21 obtained through the final inverted stiffness coefficients (C) and the P velocity surface resulting from an isotropic assumption (blue curve).

As can be observed, the isotropic assumption shows that vertical and horizontal velocities would be the same in a VTI medium, which is not valid in this anisotropy environment.

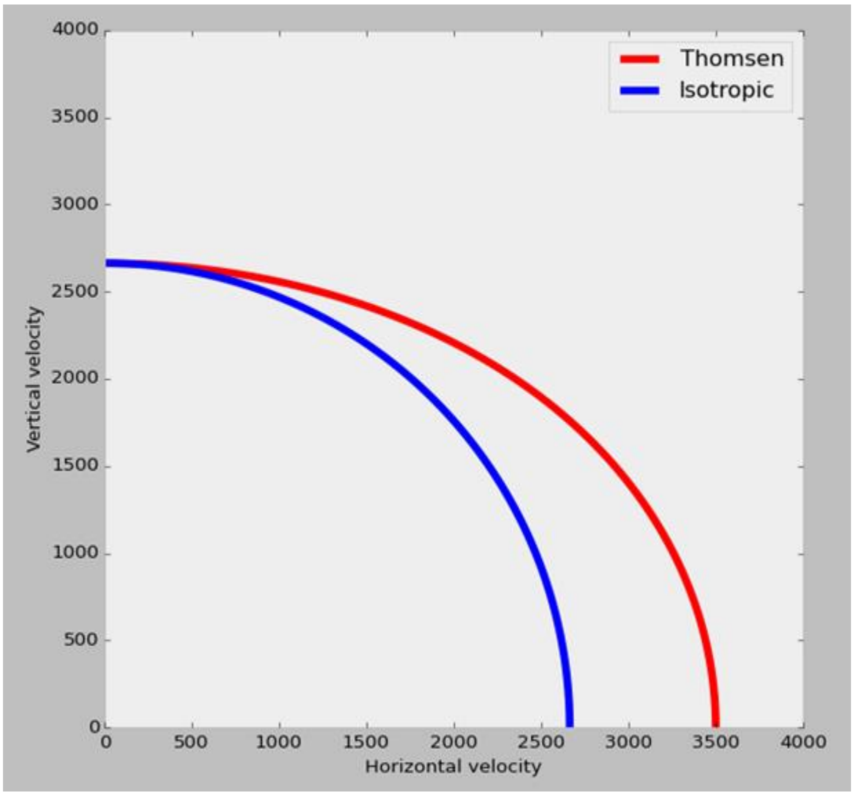

Figure 12: Polar plot. P velocities surface for inverted anisotropic parameters (red curve) and the velocity surface resulting from anisotropic assumption using the vertical well data (blue curve). As observed, the isotropic curve shows that vertical and horizontal velocities would be the same.

3.5.3 Anisotropy correction for deviated wells

Seismic events in small to medium offsets (incident angles <40°) are primarily driven by the vertical velocities. Thus, one must consider that velocity measured in highly deviated wells is strongly affected by anisotropy and not representative of the vertical velocities through the shale sections.

This section discusses a method to estimate the anisotropy-corrected vertical sonic logs using sonic data recorded in a deviated well. The method is as follows.

1. Use the inversion procedure explained in the previous section (3.5.2) to invert the stiffness coefficients C_{11}, C_{33}, and C_{44} and estimate directly the anisotropic Thomsen parameters ε and δ in a selected 100% shale interval (εsh and δsh);

2. For a particular depth, calculate the anisotropy parameters using the expressions $\varepsilon c = Vsh*\varepsilon sh$ and $\delta c = Vsh*\delta sh$, where εc and δc correspond to the final computed Thomsen anisotropy parameters, and Vsh is the volume of shale. If Vsh falls below an input *cut-off* reference value, assuming the rock to be isotropic and $\varepsilon c=0$ and $\delta c=0$;

3. From Equation 30, rewrite in terms of vertical velocity giving

$$V_{p0} \approx V_p(\theta)/(1+\delta\sin^2\theta\cos^2\theta+\varepsilon\sin^4\theta), \qquad (37)$$

4. Then, using Equation 37, calculate for each depth at their respective deviation angle a corrected vertical velocity, V_{p0}, using the previous final computed Thomsen anisotropy parameters εc and δc as input in this equation.

After correction, this vertical sonic log (corrected log) can be used for standard seismic and geomechanics processing applications.

Figure 13 shows the inversion and velocity correction results. Synthetic sonic velocities for the vertical well (Vp_MEAS) are in red, corrected vertical velocity (Vp_vertical) through the deviated well data is in blue, and the deviated TIV anisotropy affected velocity curve (VP_DESV) is in green. Comparing the corrected log with the reference vertical velocity log shows a good fit, particularly below the sand layer (100% shale section corresponding to the inverted Thomsen parameters). Thomsen parameters εc (eps) and δc (delt) are in the order of 0.31 and 0.21 respectively for the 100% shale section (bottom section) and almost zero for the isotropic sand section as expected.

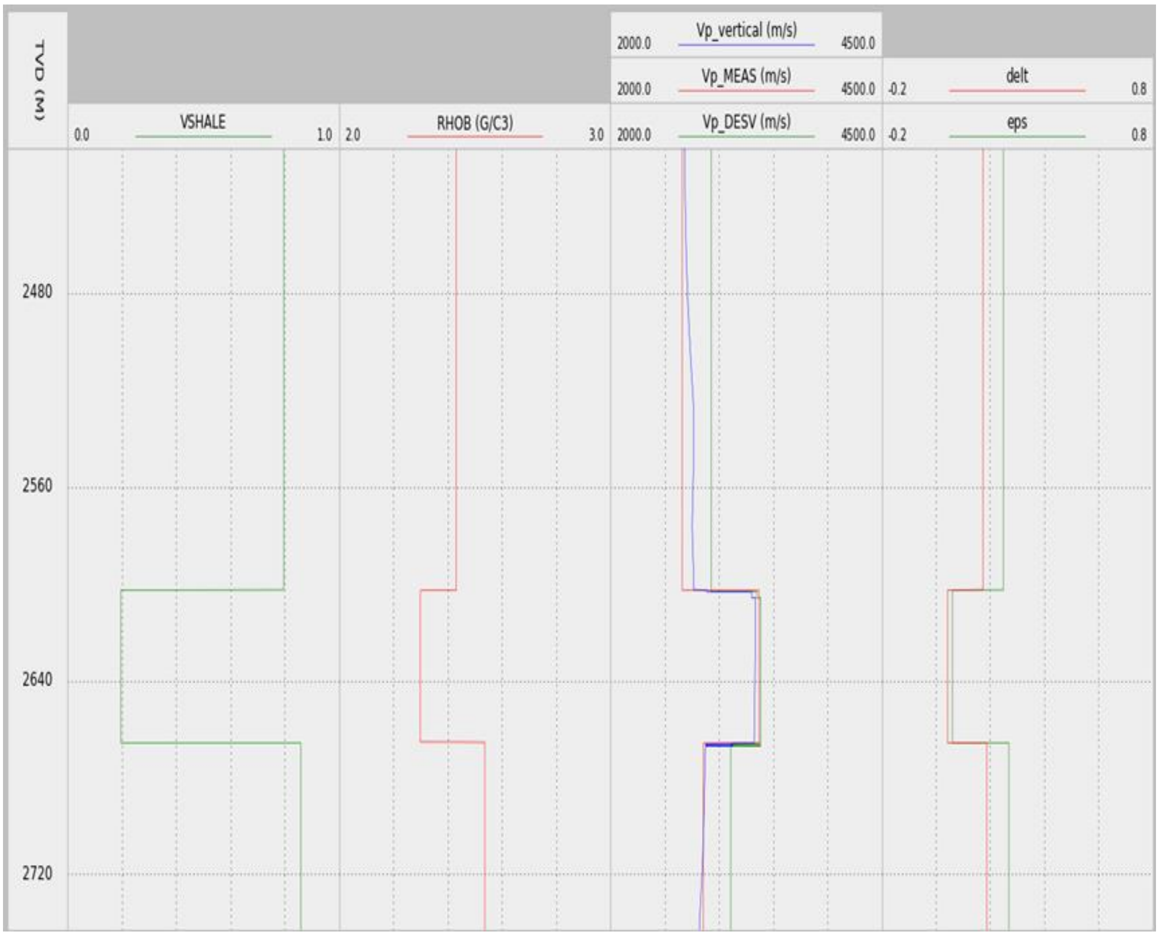

Figure 13: Synthetic model curves GR, RHOB, with Vp_MEAS and VP_DESV representing the vertical and deviated sonic velocities. Vp_vertical represents the anisotropy corrected curve; delt (δc) and eps(εc) are the final Thomsen parameters estimated through the inverted stiffness coefficients.

4. INTEGRATED ROCK PHYSICS AND GEOMECHANICAL APPROACH FOR PORE PRESSURE ESTIMATION

Traditionally, pore pressure calculation formulas have been proposed to be used on a set of wireline logs and downhole measurements. Virtually all methods rely on the principle of compaction disequilibrium and require the definition of a normal compaction trend profile, which represents the gradual decrease in porosity with increasing lithostatic pressure under normal depositional conditions. Deviations from the normal compaction trend indicate abnormal pore pressure due to some overpressure generation mechanism. Thus, pore pressure estimation methods rely on the observation that pore pressure affects compaction-dependent shale properties such as porosity, density, sonic velocity, and resistivity. This observation became the foundation of two different approaches to pore pressure prediction, which are the direct method (Hottman and Johnson, 1965; Pennebaker, 1968), and the effective stress methods, based on Terzaghi's principle (Foster and Whalen, 1966; Eaton, 1975; Lane and Macpherson, 1976; Bowers, 1999). Bowers (1999) refers to any geophysical data sensitive to pore pressure as a pore pressure indicator. Terzaghi's effective stress principle (Terzaghi, 1943) states that the differential pressure (i.e., the difference between confining and pore pressures) controls the compaction trend. Lane and Macpherson (1976) proposed separating the effective stress approaches into two classes, respectively classified as vertical and horizontal methods (see section 4.2).

The pore pressure transformation is done through semi-empirical relations based on effective stress methods developed for non-reservoir rocks (shaly formations), as presented by Hottman and Johnson (1965), Eaton (1976), and Bowers (1995). However, such relations have often been indiscriminately applied for all formation types, including reservoir sands. Taking into account these ambiguities for pore pressure estimation using conventional effective stress methods, authors, led by Carcione et al. (2002), Dvorkin et al. (2002), Sayers et al. (2003), and Doyen et al. (2004), proposed new models for pore pressure estimation in reservoir rocks, what represents an advance for the pore pressure studies. Compressional velocity plays a central role in these methods, considering it is directly affected by effective stresses. Therefore, continuous efforts have been made to obtain reliable compressional velocity data and estimates and the development of comprehensive modeling formulations.

Following this continuous effort path, we propose and test an extended forms of Bowers (1995) and Doyen et al. (2004) formulae, representing pore pressure as a function of compressional velocity, effective stress, porosity, clay, and fluids volumes, as well as pore pressure as a function of shear velocity, effective stress, porosity, and clay.

Finally, in this chapter, I show the use of an adapted nonlinear multidimensional inversion method to calibrate the proposed models and apply them in the context of a 1D geomechanics and pore pressure prediction study involving an upper cretaceous overpressured shaly sand oil reservoir. Results showed reasonable confidence when compared to the Eaton method and direct pore pressure measures.

4.1. 1D Mechanical earth model

A 1D mechanical earth model (1D MEM) generally contains a description of the elastic properties, strengths, stresses, and pressures as a function of depth. Its construction requires a sequential calibration process, which must be done as rigorously as possible using available measurements and observations to arrive at an internally consistent representation of the main geomechanical properties and parameters needed for subsequent analyses and engineering designs (Ali et al., 2003; Plumb et al., 2000). A typical workflow chart for the key 1D MEM steps is displayed in Figure 14. This figure shows the necessary and sequential workflow for constructing a 1D mechanical earth model. Pore pressure estimation (red rectangle) is critical for subsequent steps like minimum stress, maximum stress, and failure model for a consistent final wellbore stability window estimation. Figure 15 shows a schematic illustration of a 1D mechanical earth model outputs (Ali et al., 2003).

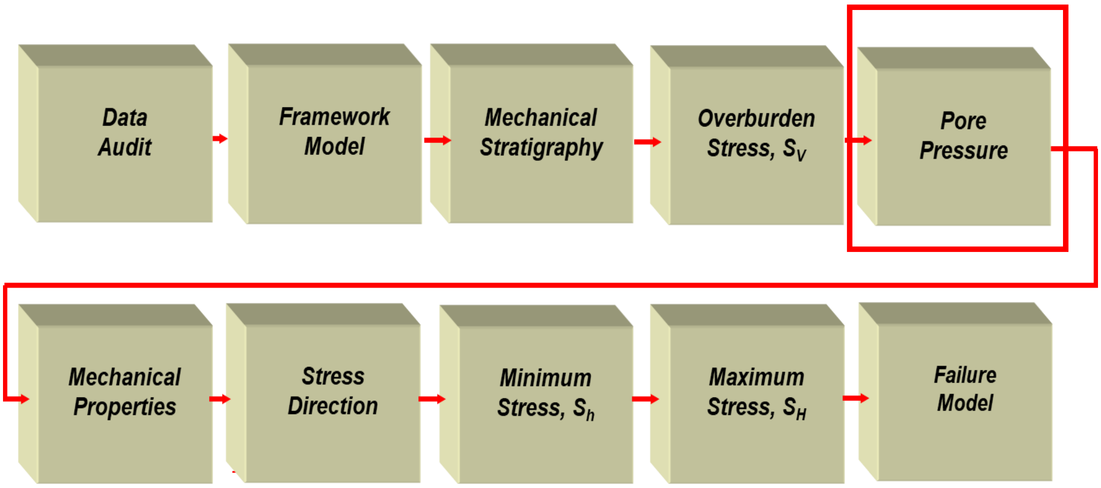

Figure 14: 1D Mechanical Earth Model sequential workflow and pore pressure step highlighted in red rectangle.

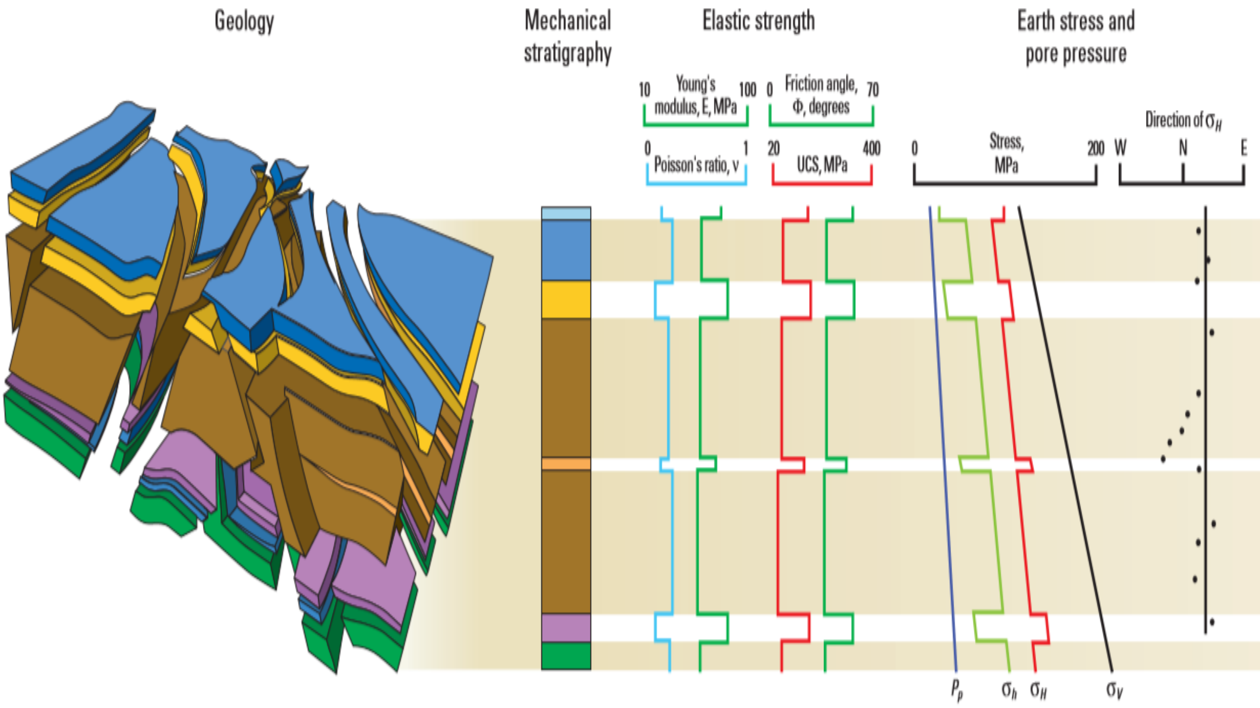

Figure 15: Schematic illustration of a 1D mechanical earth model, showing a framework model, the mechanical stratigraphy, and profiles of rock-mechanics properties, in situ stress, and pore pressure. UCS is the unconfined compressive strength, Pp is pore pressure, σ_h is minimum horizontal stress, σ_H is maximum horizontal stress, and σ_v is vertical stress (from Ali et al., 2003).

Following the mechanical Earth model (MEM) illustration in Figure 15, the first step during the MEM construction is to understand the local and regional geology (possibly considering the static model - left side of the figure). It provides a basis for the mechanical stratigraphic column using information about facies types and lithological classification during the construction (mechanical stratigraphy track in the figure). Next, the elastic and rock strength parameters, including the unconfined strength (UCS), can be estimated with their respective lithology profile as observed in the figure above. These elastic and mechanical parameters are also used to correlate and validate the vertical stress, σ_v, pore pressure, P_p, and to predict the minimum and maximum horizontal stresses. Determining horizontal stress direction is also crucial for maximizing drilling and completion operations (last track in Figure 15).

4.2. Pore pressure prediction theory

An estimate of formation pore pressure before drilling is essential for successful exploration and drilling. During the exploration phase, an estimate of pore pressure can be used to develop fluid-migration models, study the effectiveness of seals, and rank prospects. In addition, a predrill pore-pressure estimate allows selecting the appropriate mud weight and optimizing the casing design, thus enabling safe and economic drilling. Traditionally, pore pressure calculation formulas have been applied on a set of wireline logs and downhole measurements (Eaton, 1965). This section covers the basic concepts of pore pressure and the methods for estimating using elastic wave velocity measurements. Pore pressure can be estimated from seismic velocities using a velocity-to-pore-pressure transform calibrated with offset-well data (Sayers et al., 2003).

Important concepts related to geopressure include pore pressure, hydrostatic pressure, overpressure, underpressure, lithostatic pressure or overburden, and effective stress (Fig. 16). Pore pressure or formation pressure refers to the pressure of the fluid contained in the pore spaces of the sediment or other rock. Hydrostatic or normal pore pressure is the pressure exerted by the weight of a static column of fluid between the measurement point and the atmosphere. This pressure is a function of average fluid density, and the vertical height or depth of fluid column and their magnitude can vary with the concentration of dissolved salts, type of fluid, gas present, and temperature gradients. Mathematically it is expressed as

$$P_N = g.\rho_f.h \ , \tag{38}$$

where P_N is the hydrostatic pressure, g is the acceleration due to gravity, ρ_f is the density of the fluid, and h is the True Vertical Depth (TVD). Overpressure or abnormal pressure is when the pore pressure exceeds the hydrostatic pressure at a given depth. Underpressure or subnormal pressure is when the pore pressure is less than the hydrostatic pressure at a given depth.

Lithostatic pressure or overburden is the pressure exerted by the total weight of the overlying formations above the point of interest. It is a function of bulk density. Mathematically for a depth z, it is expressed as

$$\sigma_v(z) = \int_0^z \rho(z) g dz \ , \tag{39}$$

where $\rho(z)$ is the bulk rock density and g is the acceleration due to gravity. For offshore environments, the column of seawater weight must be added to give

$$\sigma_v(z) = \int_{z_w}^z \rho(z) g dz + \rho_w g z_w \ , \tag{40}$$

where z_w is the column of water height (depth to the ocean floor) and ρ_w is the water density. In Figure 16 (graphic created for this thesis), effective stress is the pressure supported by the rock matrix, as described in the following sections.

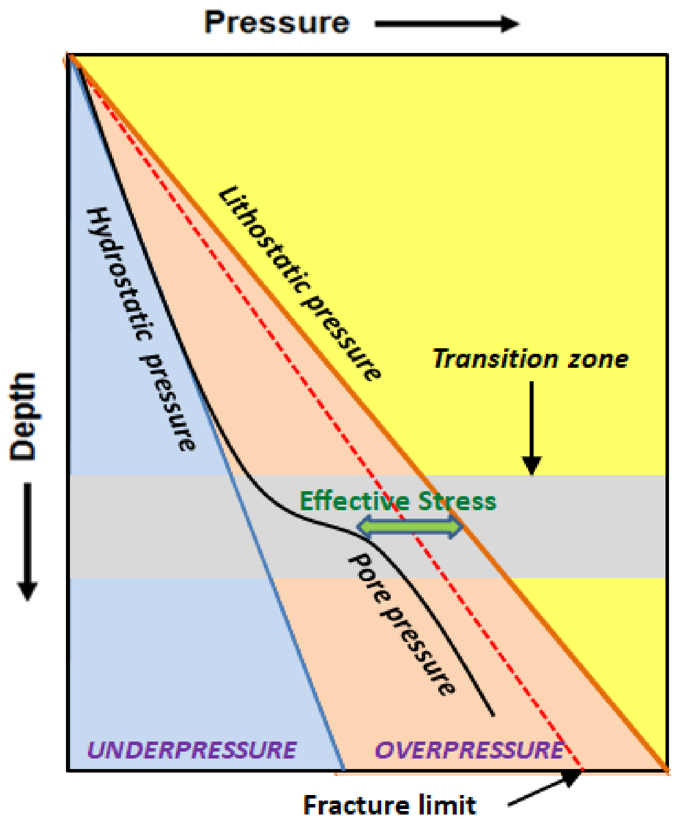

Figure 16: Graphical representation of Geopressures.

Underpressure	P_G < 8.5 ppg
Normal pressure	8.5 ppg < P_G < 9.0 ppg
Overpressure	9.1 ppg < P_G < 90% σ_g
High overpressure	P_G > 90% σ_g

Table 4: Pore pressure gradients classification. From Rocha and Azevedo (2009).

Table 4 gives us some reference of pressure magnitudes in terms of the pore pressure gradient (P_G) in ppg units, also considering the overburden gradient term (σ_g) and following previous geopressures definitions.

4.2.1. Pore pressure estimation methods

Pore pressure can be estimated from elastic wave velocities by using a velocity-to-pore-pressure transform. Early examples include the work of Hottman and Johnson (1965) using sonic velocities, as well as Pennebaker (1968) using seismic interval velocities obtained from stacking velocities. Most velocity-to-pore-pressure transforms are based on the effective stress principle given by Terzaghi (1943). The effective stress principle states that all measurable effects of a change in stress — such as compaction and variation in elastic wave velocities — are functions only of the effective stress. As highlighted in this section, it is also important to note that seismic and 1D geomechanics pore pressure approaches differ in processing considerations. All pore pressure estimation methods stand on the premise that pore pressure influences compaction-dependent shale properties such as porosity, density, sonic velocity, and resistivity. Any wireline or geophysical measurement sensitive to pore pressure serves as a "*pore pressure indicator"* (Bowers, 1999). There are two general approaches for converting pore pressure indicator measurements into pore pressure estimates that is described in subsequent sections:

- Direct Methods
- Effective Stress Methods

4.2.2. Direct methods

Direct methods relate the amount a pore pressure indicator diverges from its normal trend line to the pore pressure gradient in their respective depth of analysis. There are two direct methods given by Hottman and Johnson (1965) and Pennebaker (1968), respectively. Hottman and Johnson's method (1965) uses a cross plot for both resistivity and sonic transit time to relate departures from the normal trend line of a pore pressure indicator to the pore pressure gradient at that depth. Regional well-log data and pore pressure measurements are used to fit a measure of normal trend departure (X-axis) against the pore pressure gradient (Y-axis). Cross plot patterns reflect the geologic conditions of the studied area. Mathews and Kelly (1967) have found that Hottman and Johnson's original Gulf Coast sonic transit time cross plot generally provides an upper bound for pore pressure in most Tertiary basins but overestimates pore pressure in areas of deepwater Gulf of Mexico.

Pennebaker (1968) focuses on pore pressure prediction from seismic interval transit times. As Hottman and Johnson's original cross plot (1965), Pennebaker's approach was based primarily upon well data from the Texas and Louisiana Gulf Coast. However, he includes different geologic ages and even different lithologies in order to generalize his method. He assumes that a formation interval transit time normal trend follows the same slope when plotted versus depth on a log-log plot. A change in geologic age and lithology (differential diagenetic process) would cause the normal trend to undergo a lateral shift parallel to the interval transit time axis. Therefore, he assumes in his approach that one overlay could be applied worldwide by simply shifting it to account for lithology/age/diagenetic process changes. Over the years, it has become apparent that one worldwide pore pressure overlay is generally not sufficient for any given pore pressure indicator (Bowers, 1999).

4.2.3. Effective stress methods

Effective stress methods, as defined previously, are based upon Terzaghi's effective stress principle (Terzaghi, 1943), which states that the compaction of geologic materials is controlled by the difference between the total confining pressure and the pore fluid pressure. This difference, termed the effective stress, represents the portion of the total stress carried by the rock or sediment grains as expressed by the equation

$$\sigma_v' = \sigma_v - P_p, \tag{41}$$

where σ_v and P_p are the absolute vertical stress (overburden) and pore pressure, respectively. Essentially, effective stress methods consist of three steps:

1. The vertical effective stress (σ_v') is estimated from a pore pressure indicator measurement.
2. The overburden stress (σ_v) is determined from measured or estimated bulk density data.

3. Arranging Equation 4, the pore fluid pressure (P_p) is obtained from the difference

$$P_p = \sigma_v - \sigma_v' \, , \tag{42}$$

All new pore pressure methods published since the late '60s have been effective stress approaches. They differ only in the way that they determine effective stresses. Following Bowers (1999), these techniques can be subdivided into three categories that will be described in subsequent sections:

1) Vertical Methods
2) Horizontal Methods
3) Other

4.2.3.1. Vertical, horizontal and other methods

Lane and Macpherson (1976) first suggested categorizing pressure techniques as horizontal or vertical methods. Later Bowers (1995) developed his version of the vertical method, classified in the "other" category. Table 5 categorizes various pore pressure estimation methods that have been published for sonic velocity-transit time (Bowers, 1999). Hottman & Johnson's (1965) direct methods used cross plots to relate departures from the normal trend line of a pore pressure indicator (sonic transit times) to the pore pressure gradient at that depth of interest, not including overburden dependence in their approach (without effective stress relations). Vertical methods, such Equivalent Depth method by Foster and Whalen (1966), compute equal effective stress in depths with the same pore pressure indicator value (e.g., the same velocity) following the normal trend reference for the respective depth of interest (see Figure 17).

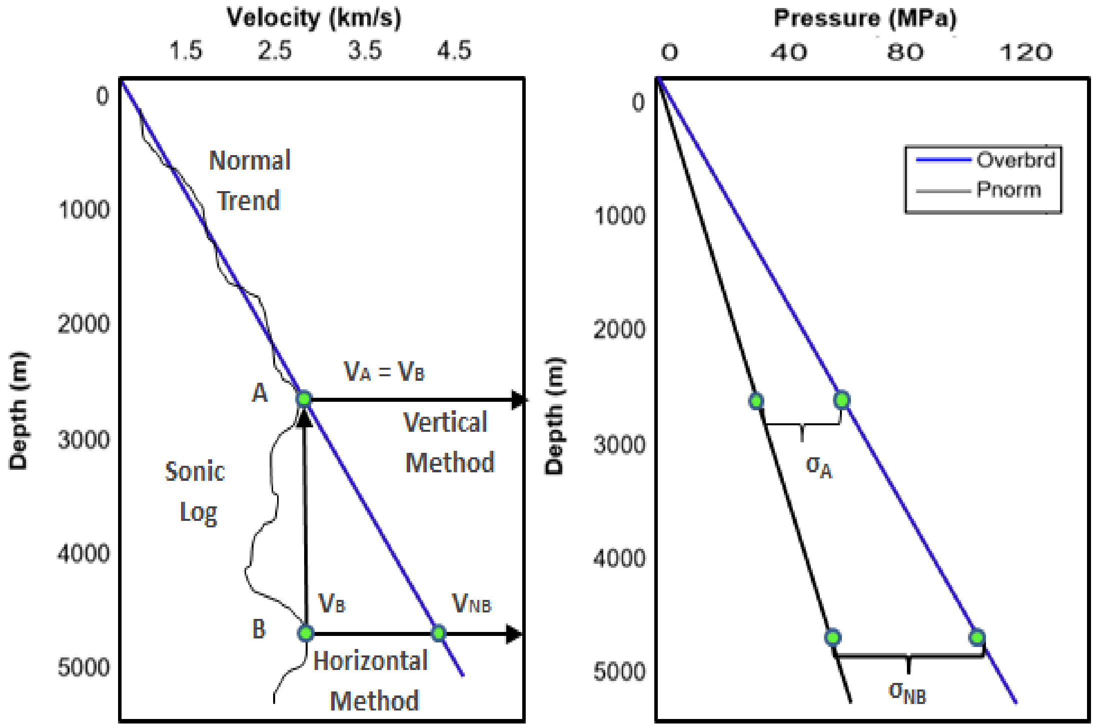

Figure 17: Vertical vs. horizontal pore pressure estimation methods (Left figure: sonic or interval velocity vs depth; Right figure: pressure vs. depth). Having Point A and Point B with the same velocities (V_A=V_B), vertical methods use the fitted velocity normal trend data (blue curve in left figure) with Point A as depth reference for effective stress computation at the depth of Point B (assuming equal values $\sigma_A = \sigma_B$ in the right figure where blue and black curves represent the overburden and normal pressure curves). Horizontal methods would use the normal trend data at the respective depth of interest (Point B) where measured velocities are not the same as the normal velocity (V_B≠V_{NB}) to compute their respective effective stress (σ_{NB}). Modified from Bowers (1999).

Horizontal methods, such as Eaton's Method (Eaton, 1975), compute non-equal effective stress from normal trend data at the same depth of their pressure indicator and the respective depth of interest (see also Figure 17). "Others" effective stress methods category like Bowers (1999) applied for cases, where normally pressured and overpressured formations do not follow the same, unique relation for compaction as a function of effective stress. Therefore, it can be viewed as a "modified" Equivalent Depth method. Effective methods like Eaton's and Bower's sonic methods are the most widely used approaches in the industry (Yoshida et al., 1996). These two methods are described in the following subsections.

Direct	Effective stress		
	Vertical	Horizontal	Other
Sonic • Hottman & Johnson	Sonic • Equivalent Depth	Sonic • Eaton	Sonic • Bowers

Table 5: Classification of main published sonic pore pressure estimation methods (Bowers, 1999).

4.2.3.2. Eaton method

Horizontal methods like Eaton (1975) compute the effective stress from the normal velocity trend curve and the normal effective stress at a depth using the next compressional velocity relation

$$\sigma' = \sigma'_N \left(\frac{V}{V_N}\right)^n , \tag{43}$$

where the subscript N denotes the normal trend values at a depth of interest, and the n term is referred to as the Eaton exponent. For example, for the velocity at point B in Figure 18a, we have the normal velocity point V_{NB} and the corresponding normal effective stress σ_{NB} (Figure 18b) at point B. Figure 18c shows an interpretation of what Eaton's method and their respective equation are doing. The velocity V_{NB} and effective stress σ_{NB} picked on the normal trend (blue curve based on the hydrostatic pressure) determine the stress-velocity proportion used, together with V_B, to obtain the final effective stress relation σ_B. In other words, the remainder of the curve between (V_{NB}, σ_{NB}) and (V_B, σ_B) is then approximated with Equation 43.

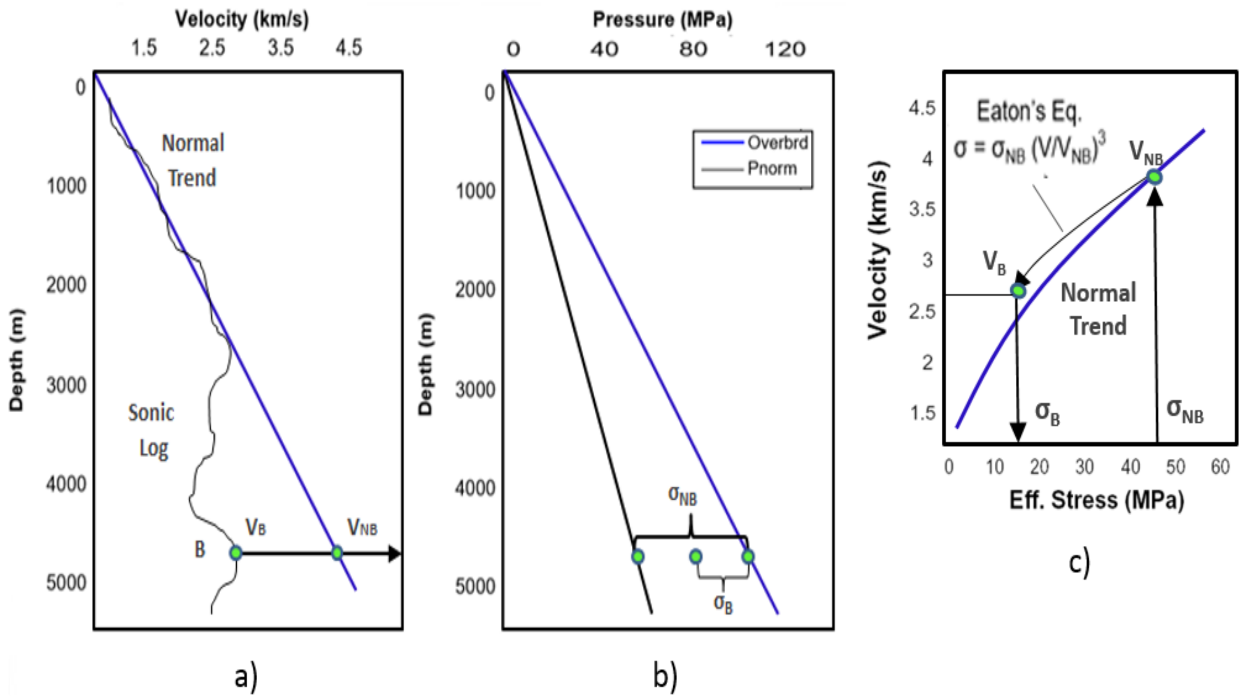

Figure 18: Horizontal effective stress methods - Eaton's method. Modified from Bowers (1999).

In Figure 18c, when the normal compaction trend has a shape similar to Eaton's equation trend, the effective stresses calculated in the overpressure reversal zone with Eaton's method are close to the true compaction trend. In this case, Eaton's and vertical effective stress methods listed in Table 5 produce similar results. However, as the shape of the normal trend curve diverges from Eaton's trend, so do the overpressures results computed with Eaton's method and vertical methods (Bowers, 1999).

4.2.3.3. Bowers method

Bowers' method (Bowers, 1995) can be viewed as a modified Equivalent Depth method. As illustrated in Figure 19, effective stresses are calculated at two points along the normal trend curve: 1) the standard equivalent depth Point A, and 2) the point where the velocity curve reaches its peak value V_{MAX}. The effective stress at Point B is given by

$$\sigma'_B = \sigma'_{MAX} \left(\frac{\sigma'_A}{\sigma'_{MAX}}\right)^U , \tag{44}$$

where σ'_A is the effective stress at the equivalent depth A, σ'_{MAX} is the effective stress corresponding to V_{MAX} and U is calibrated using well-log data (direct pore pressure measures). For the Gulf Coast and the Gulf of Mexico, U = 3.13 (Bowers, 1995).

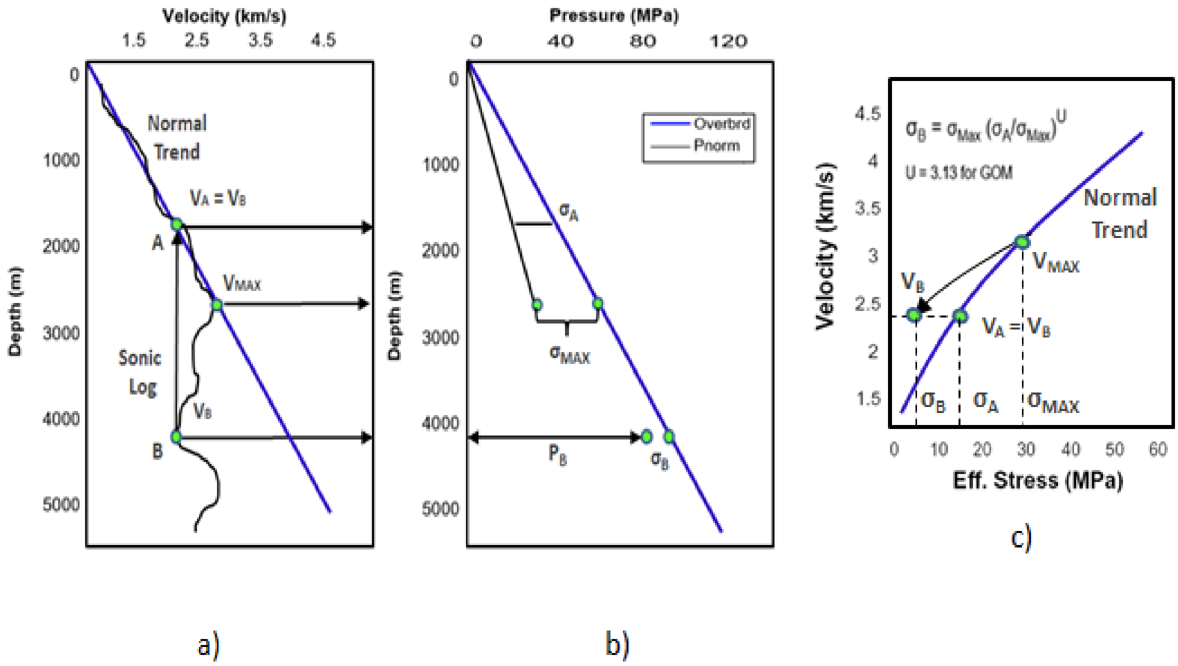

Figure 19: Bowers pore pressure estimation method. Modified from Bowers (1999).

As shown in Figure 19c, Equation 44 places the reversal velocity (reversal begins at 2700 m approximately as observed in Figure 19a) onto a faster compaction curve. A similar effect can be accomplished by increasing the Eaton exponent. To avoid having to solve for σ'_A and σ'_{MAX} graphically, Bowers (1995) introduced an analytical relation

$$\sigma_v' = \left(\frac{V_p - V_{p0}}{A}\right)^{\frac{1}{B}}, \tag{45}$$

where σ_v' is the vertical effective stress, V_p is the measured compressional velocity, V_{p0} is the zero-stress mudline velocity, and A and B are calibration parameters to be adjusted with well-log data (direct pore pressure measures). Reversal velocity zones indicate potentially high overpressures, and when such overpressures occur, the reversal velocity data deviate from the normal compaction trend on the effective stress plot (Bowers, 1995), as observed in the example illustrated in Figure 19c. However, not always reversal zones have ultra-high pore pressure. Considering that Eaton and Bowers methods are suitable for clastic sequences as they have been developed using data from GoM, reversal data sometimes track the same effective stress trend as lower pressured and normally pressured intervals. All pore pressure estimation methods classified as "Other" like Bowers attempt to account for cases where overpressure data track different trend.

4.2.3.4. Sayers method

Sayers et al. (2003) introduce a method for pore pressure estimation in sands using interval velocities obtained from seismic reflection tomography through the following expression:

$$P_P = \sigma_v - \left(\frac{V_p - V_{p0}}{A}\right)^{\frac{1}{B}}, \tag{46}$$

where P_P is the pore pressure, σ_v is the absolute effective stress, V_p is the measured compressional velocity, V_{p0} is the zero-stress mudline velocity, and A and B are calibration parameters as defined in the previous section. Equation 46 that is the same expression of Bowers (Eq. 45) can be rearranged as a function of compressional velocity and effective vertical stress for better handling during the calibration process:

$$V_P = V_{P0} + A(\sigma'_v)^B, \tag{47}$$

Equation 47 must be calibrated in sand intervals containing the same or similar fluids. In other words, V_{P0} and the coefficients A and B are calibration parameters for the model to work in sand regions with the same fluid content. Calibrations follow the same procedure used in 1D geomechanics pore pressure estimation with well-logs and Bowers method, including for the Sayers method a sonic "*upscaled"* compressional velocity, overburden estimation from the vertical integration of density and pore pressure direct measurements obtained from well-testing tools or LWD/WL logging tools.

4.2.3.5. Doyen method

Doyen et al. (2004) introduce a probabilistic method using either a linearized Gaussian approximation or a sequential stochastic simulation approach that fully accounts for nonlinearities and uncertainties in the velocity to pore pressure transform and spatial correlation between the different input variables.

This pore pressure estimation method represents an evolution of the previous method (Sayers et al., 2003), extending Bowers formula to link pore pressure and seismic velocity, overburden stress, porosity, and clay volume to get

$$V_p = a_1 - a_2\emptyset - a_3C + a_4(\sigma'_v)^{a_5} \ , \tag{48}$$

where a_i are the model coefficients, whose values are determined by calibration using well-log data, $\emptyset$ is the porosity, C the volume of shale and σ'_v the vertical effective stress. In the above equation, the velocity dependence on differential (or effective) stress, given by σ'_v is equivalent to the expression proposed by Bowers (1995), where the zero-stress mudline velocity term V_{P0}, in Equation 47, are given analogously by $a_1 - a_2\emptyset - a_3C$ to account for variations in porosity and lithology in this case. This equation can be arranged to obtain an expression for the pore pressure, written as

$$P_P = \sigma_v - \left[\frac{1}{a_4}\left(V_p - a_1 + a_2\emptyset + a_3C\right)\right]^{\frac{1}{a_5}} , \tag{49}$$

Equation 49 may be applied point-by-point in a 3-D MEM (mechanical earth model), assuming that a velocity, porosity, and clay volume area available from previous seismic inversion and reservoir characterization workflows (Doyen et al., 2004).

In practice, the velocity to pore pressure transform calibration is required for each formation and fluid type, as prescribed before (Sayer et al., 2003).

4.2.3.6. Eberhart-Phillips method

Eberhart-Phillips et al. (1989), following the studies done by Han (1986), used a multivariate analysis to investigate the influence of effective pressure P_e, porosity $\emptyset$, and clay content C on compressional velocity V_p and shear velocity V_S. Laboratory measurements on water-saturated samples of 64 different sandstones provide a data set for statistical analysis, resulting in V_p and V_S relations to effective pressure.

The samples have an exponential increase in velocity at low P_e tapering to a linear increase for P_e greater than 0.2 kbar. The best-fitting formulations for the combined set of measurements from all samples, obtained by Eberhart-Phillips, gave the following velocity relations:

$$V_p = 5.77 - 6.94\emptyset - 1.73\sqrt{C} + 0.446(P_e - e^{-16.7P_e}), \quad (50)$$

and

$$V_S = 5.77 - 6.94\emptyset - 1.73\sqrt{C} + 0.446(P_e - e^{-16.7P_e}),. \quad (51)$$

It is remarkable how well the velocity of the clastic rocks considered in these formulations can be predicted based on these three parameters $\emptyset$, C, and P_e, which can also be used for velocity pore pressure transformation.

4.3. Judgment of Abnormal Overpressure Cause

The causes of pore pressure is a broad topic of discussion as can be found in several publications with their respective theories on this subject (Bowers, 1999; Fertl and Chilingarian, 1977; Martinsen, 1994; Mouchet and Mitchell, 1989; Law and Spencer, 1998; Swarbrick and Osborne, 1994; Zoback, 2010). This section presents a compilation of concepts based on these previous works and definitions used by Zhu et al. (2011).

4.3.1. Loading and unloading

The causes of abnormal pore pressure can be related to the loading and unloading process (Jin et al., 2000). During the normal loading process, the rock framework's effective stress increases with the increase of the overburden stress.

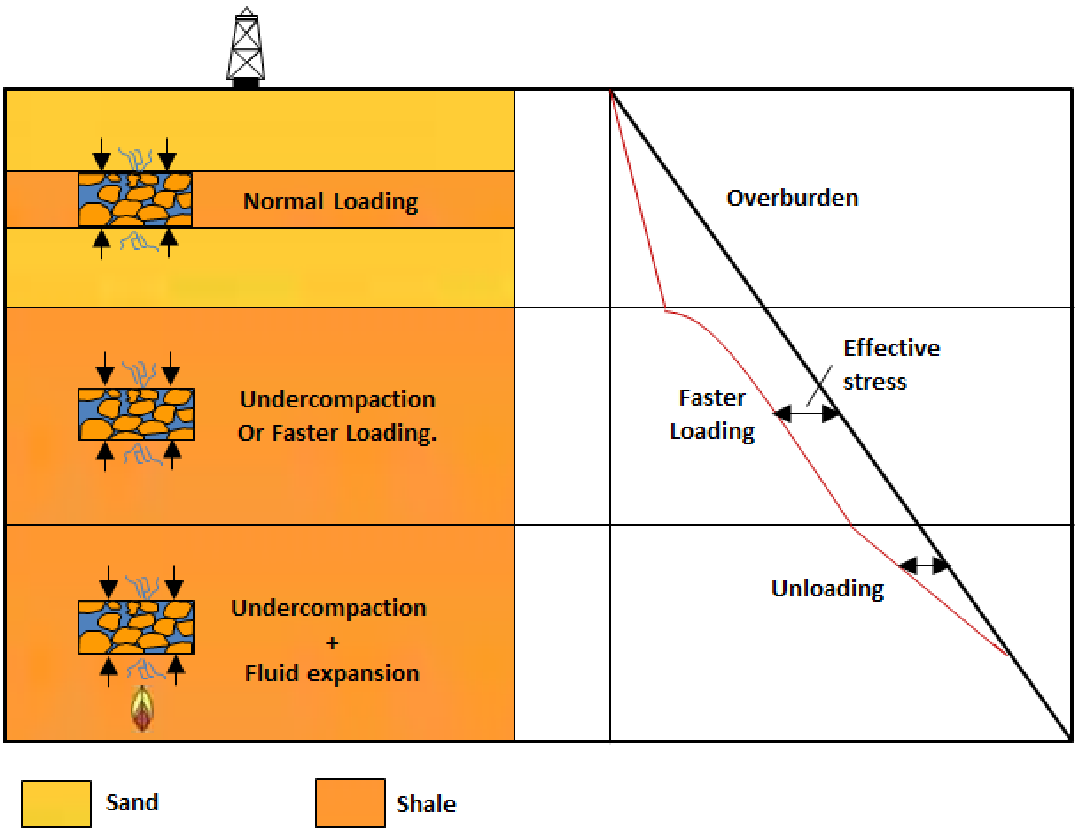

Figure 20: Illustration of primary overpressure mechanism (modified from Bowers, 2002).

To distinguish different loading regimes is helpful to define what we consider normal pressures ("normal loading") and abnormal pressures ("faster loading"). During faster loading or undercompaction, effective stress is maintained constant, as shown in Figure 20. However, when the formation properties change with structural tectonic movements or a fluid expansion occurs together with undercompation, the original rock framework's effective stress may reduce drastically, and this process is called unloading (see Fig. 20). Unloading mechanisms commonly generate reversal effects in seismic velocities.

4.3.2. Cause of abnormal overpressure

Abnormal pore pressure studies should consider the levels of compressibility of the rock and their respective fluids, especially during faster loading (ex. undercompaction). If the rocks are more compressible than the pore fluid (young and shallow formations), the stress becomes supported by the fluid. On the other hand, if the pore fluid is more compressible than the rock, the stress becomes supported by the rock (old and deeper formations). Following previous definitions, undercompaction could be the dominant abnormal pore pressure mechanism for shallower young formations where rocks tend to be less consolidated. Table 6 shows a relation between the abnormal overpressure cause and their respective mechanical mechanism relation considering the loading and unloading process (Zijian Chen et al., 2015).

<table>
<tr><th colspan="2">Cause of abnormal overpressure</th><th>Mechanical mechanism</th></tr>
<tr><td>The change of pore volume</td><td>Undercompaction</td><td rowspan="2">Loading</td></tr>
<tr><td rowspan="3">The structural tectonic movement</td><td>Compression from in-situ stress</td></tr>
<tr><td>Shear from in-situ stress</td><td rowspan="9">Unloading</td></tr>
<tr><td>Uplift of the formation</td></tr>
<tr><td rowspan="6">The change of formation pore fluid volume</td><td>Aquathermal expansion</td></tr>
<tr><td>Clay diagenesis</td></tr>
<tr><td>Hydrocarbon generation</td></tr>
<tr><td>Fluids migration</td></tr>
<tr><td>Permeation</td></tr>
<tr><td>Hydraulic head</td></tr>
</table>

Table 6: Relation between the abnormal overpressure cause and their respective mechanical mechanism. Adapted from Zijian et al. (2015).

Loading mechanism classification in Table 6 corresponds precisely to the called faster loading process defined previously.

In the normal compaction or normal loading, the rock framework's effective stress increases with the buildup of overburden pressure (Fig. 20), and the pore pressure remains equal to the hydrostatic pressure. However, for the undercompaction regimen, the pore pressure becomes higher than the hydrostatic pressure with increasing overburden pressure because the formation fluid cannot outflow normally.

At the same time, the effective stress decreases to be nearly constant, as shown in Figure 20. Therefore, the undercompaction also generally belongs to the loading process, as indicated in Table 6. Furthermore, the intense structural tectonic movement, leading to a strong compression from the horizontal stress, also results in abnormal overpressure. The mechanical mechanism is the same as the undercompaction, just the loading direction changes from the vertical direction to the horizontal direction. Thus the intense structural tectonic movement is also regarded as a loading process (in this case, also placed in the faster loading process category).

The abnormal overpressure develops after the formation compaction in hydrocarbon generation, aquathermal expansion, and clay diagenesis. Consequently, the pore pressure increases and the effective stress is progressively reduced, as seen in Figure 20. Hence, the change of formation pore fluid volume belongs to the unloading process. Furthermore, the structural shear action caused by the variation of in-situ stress breaking the pore can also cause effective stress to be reduced, thus contributing to the unloading process.

4.4. Pore pressure estimation method following proposed equations

The previous section showed how Terzaghi's effective stress principle (Terzaghi, 1943) is central for understanding pore pressure control and abnormal pore pressure mechanisms. Here we discuss how the different methods can be applied in pore pressure estimation.

4.4.1. Direct pore pressure workflow estimation

The integrated approach to pore pressure estimation requires an entire workflow involving wave propagation velocities, porosity, shale fraction, as well as information on overburden pressure and fluid content derived from well data and perhaps seismic data. Also, model equations must be properly calibrated to yield a formula that can be used to predict the pore-pressure profile (Fig. 21).

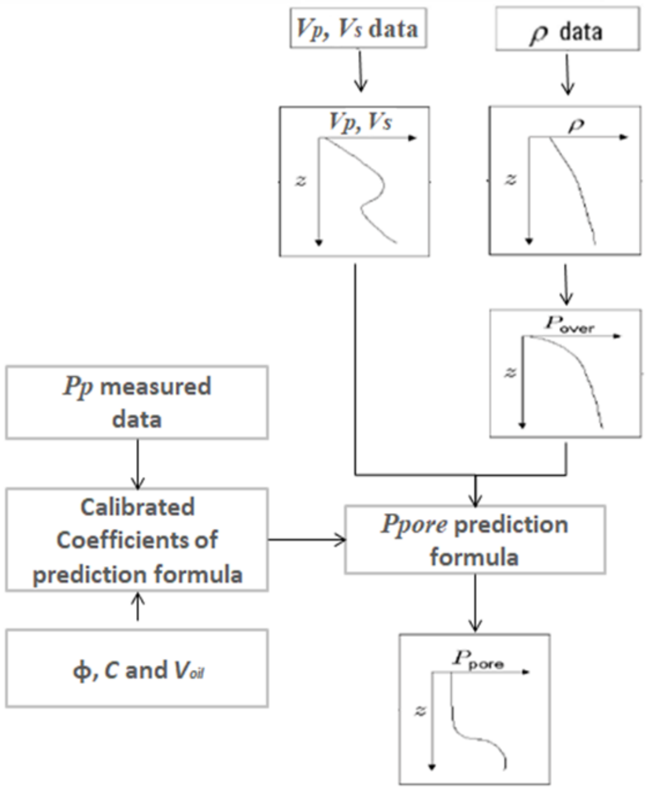

Figure 21: Basic workflow for predicting pore pressure through Equation 49 or 50, using well-log or seismic derived velocities, density and petrophysical parameters.

The direct proposed (or deterministically) pore pressure estimation sequence can be described, in more detail, by the following steps:

1. Construct the best velocity $V_p(z)$ or $V_s(z)$, and density $\rho(z)$ depth profiles.

2. Use the density $\rho(z)$ to estimate the total vertical stress or overburden pressure P_o (Eq. 20).

3. Petrophysical interpretation – compute clay volumes, effective porosity and saturation (i.e., mineral and fluid solver analysis) using wireline or LWD data, and perform lithologic interpretation discriminating the shales and cleaner intervals.

4. Calibrate model coefficients – use the results of the previous step, together with pore pressure data, to obtain coefficients $\boldsymbol{a_i}$ or $\boldsymbol{b_i}$, as in Equations 16 and 17 using a preferred regression algorithm.

5. Compute the predicted pore pressure $\boldsymbol{P_P}$ for sand and shaly sand sections, using Equation 18 or 19 with inputs from the previous steps, and compare predicted and measured pore pressure values using mud weight for quality control purposes.

Considering the semi-empirical nature of the proposed formulations, it is always important to check against competing approaches, such as represented by Eaton's method (Eaton, 1975).

4.4.2. Non-linear inversion for pore pressure calibration

To perform step 4 of the workflow presented above, I also implemented a non-linear inversion sequence approach to obtain the calibrated coefficients, $\boldsymbol{a_i}$ and $\boldsymbol{b_i}$**,** of the pore pressure velocity relations defined in Equations 16 and 17. This is calibration step is traditionaly done graphically by the interpreter, but a more formal approach is to solve a nonlinear least-squares minimization problem with the Levenberg-Marquardt (LMA) using the numerical Scipy library.

As with many gradient-based algorithms, the LMA finds only a local minimum, not necessarily the global minimum. This algorithm combines two minimization methods: the gradient descent and the Gauss-Newton methods. In the gradient descent method, the sum of the squared errors is reduced by updating the parameters (in our case, the calibration coefficients) in the steepest-descent direction.

In the Gauss-Newton method, the sum of the squared errors is reduced by assuming the least-squares function as *locally quadratic* and finding the minimum of the quadratic. We could say that, in general terms, the Levenberg-Marquardt method acts similar to a gradient-descent method when the parameters are far from their optimal value and acts similar to the Gauss-Newton method when the parameters are close to their optimal value (Gavin, 2011). The LMA, in many cases, finds a solution even if it starts very far off the final minimum been more robust than the GNA in several optimization scenarios. The algorithm is attributed to Levenberg K. (1944) and Marquardt D. (1963).

The primary application of the Levenberg–Marquardt algorithm is in the least-squares curve-fitting problem. In fitting a function $\hat{y}(t;\boldsymbol{p})$ of an independent variable t and a vector of n parameters p to a set of m data points (t_i, y_i), it is convenient to minimize the sum of the weighted squares of the errors (or weighted residuals) between the measured data y_i and the curve-fit function $\hat{y}(t;\boldsymbol{p})$.

$$X^2(\boldsymbol{p}) = \sum_{i=1}^{m} \left[\frac{y(t_i) - \hat{y}(t;\boldsymbol{p})}{\sigma_{y_i}}\right]^2, \tag{52}$$

$$= \left(y - \hat{y}(\boldsymbol{p})\right)^T \boldsymbol{W}\left(y - \hat{y}(\boldsymbol{p})\right), \tag{53}$$

$$= y^T \boldsymbol{W} y - 2y^T \boldsymbol{W} \hat{y} + \hat{y}^T \boldsymbol{W} \hat{y}, \tag{54}$$

Equation 52 shows a scalar-valued goodness-of-fit measure called the chi-squared error criterion (Gavin, 2011), because the sum of squares of normally distributed variables is distributed as the chi-squared distribution where σ_{y_i} is the measurement error for measurement $y(t_i)$. Equations 53 and 54 represent the same expression of Equation 52, where typically the weighting matrix $\boldsymbol{W}$ is diagonal with $\boldsymbol{W_{ii}} = \boldsymbol{1}/\sigma_{y_i}^2$. More formally, $\boldsymbol{W}$ can be set to the inverse of the measurement error covariance matrix, in the unusual case that it is known. More generally, the weights $\boldsymbol{W_{ii}}$, can be set to pursue other curve-fitting goals.

If the function $\hat{y}(t;\boldsymbol{p})$ is nonlinear (as in the case of Equations 16 and 17) in the model parameters $\boldsymbol{p}$, then the minimization of X^2 with respect to the parameters must be carried out iteratively. The goal of each iteration is to find a perturbation h to the parameters $\boldsymbol{p}$ that reduces X^2 shown in Equation 52.

For moderately-sized problems, the Gauss-Newton method typically converges much faster than gradient-descent methods (Marquardt, 1963). The resulting normal equations for the Gauss-Newton update are

$$[\boldsymbol{J}^T\boldsymbol{W}\boldsymbol{J}]\, h_{GN} = \boldsymbol{J}^T\boldsymbol{W}(y - \hat{y}), \tag{55}$$

where h_{GN} correspond to the parameter update $\boldsymbol{h}$ following the Gauss-Newton method. The Levenberg-Marquardt algorithm adaptively varies the parameter updates between the gradient descent update and the Gauss-Newton update,

$$[\boldsymbol{J}^T\boldsymbol{W}\boldsymbol{J} + \boldsymbol{\lambda}\boldsymbol{I}]\, h_{LM} = \boldsymbol{J}^T\boldsymbol{W}(y - \hat{y}), \tag{56}$$

where $\boldsymbol{I}$ is the identity matrix, giving as the parameter update increment h_{LM} to the estimated parameter vector $\hat{y}$, and $\boldsymbol{\lambda}$ represent the called *damping parameter*. Small values of the damping parameter $\boldsymbol{\lambda}$ result in a Gauss-Newton update and large values of $\boldsymbol{\lambda}$ result in a gradient descent update.

Once the optimal curve-fit parameters are determined, parameter statistics like the measurement error covariance matrix (inverse of $\boldsymbol{W}$ in Equation 56) are also computed for the converged solution.

As an additional comment, a similar damping factor appears in *Tikhonov* regularization, which is used to solve linear ill-posed problems, as well as in *ridge* regression, an estimation technique in statistics. See also Tarantola (2004).

4.5 Case study and results

To test the workflow presented in the previous section, I use an idealized case study involving a consolidated upper cretaceous shaly sand oil reservoir, whose data are subjected to a confidentiality agreement.

4.5.1 Direct method

The interval analyzed shows abnormal pressures (abnormal means above local hydrostatic pressure). The data used in this study consists of clay volume, porosity, water saturation (petrophysical processed curves), compressional and shear slowness, density logs, direct measures of pore pressure, and mud weight. This *direct* method (or deterministic method) was applied using the available well-log data and following Bowers conventional power-law curve fitting approach (Sayers, 2003) following the steps described in section 4.4.1.

The model calibration in these called direct method (or deterministic method) was done by adjusting a power-law fitting with the effective pressures, PP_ef (that represent the overburden with substracted direct measures of pore pressure displayed with blue points in Figures 22 and 23) vs. V_DIFF and VS_DIFF (that represent $\boldsymbol{V_p}$ -$\boldsymbol{V_o}$ and $\boldsymbol{V_s}$ -$\boldsymbol{V_o}$ respectively, following Bowers formulation, taking into account that in the proposed formulations, $\boldsymbol{V_o}$ is linked with the petrophysical parameters as explained in section 4.2).

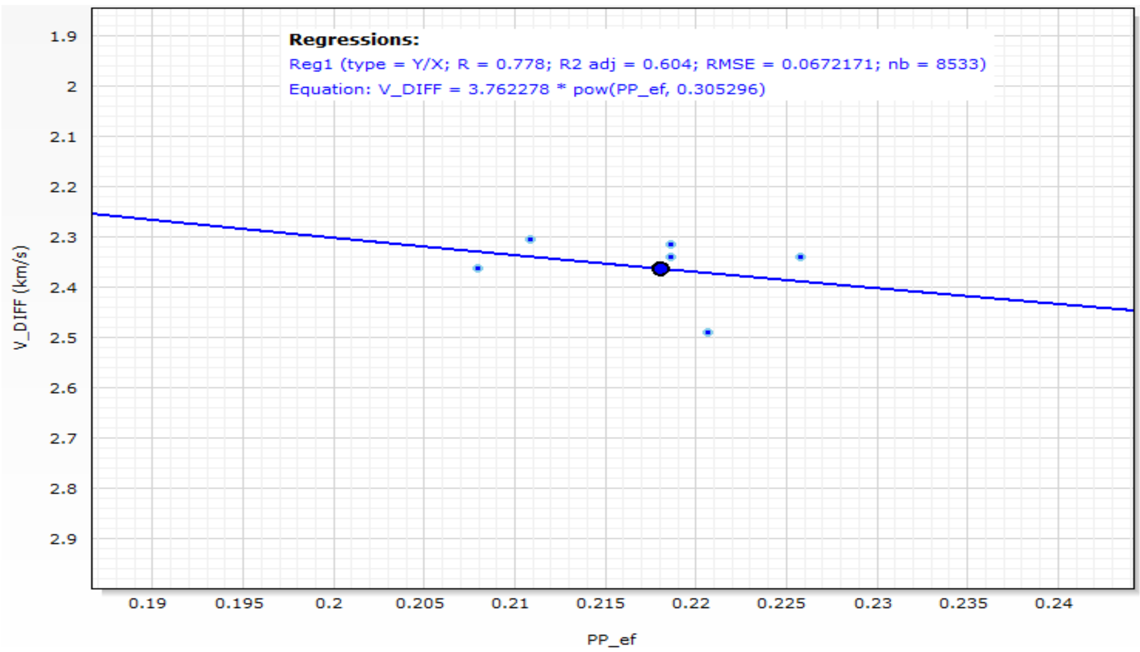

Figure 22: Direct calibration coefficient process through power-law fitting using PP_ef in Kbars units that represent the overburden subtracting direct pore pressure measures (blue dots) vs. V_DIFF in Km/s (that would represent v_p -v_o following Bowers formulation).

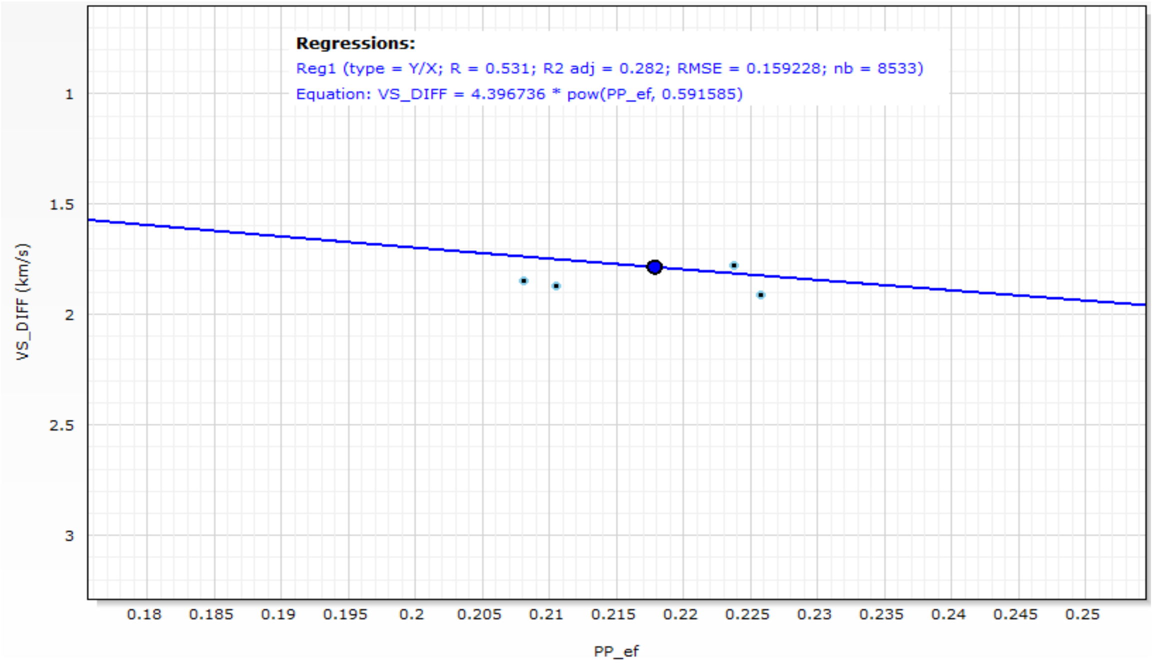

Figure 23: Direct calibration coefficient process through power-law fitting using PP_ef in Kbars units that represent the overburden subtracting direct pore pressure measures (blue dots) vs. VS_DIFF in Km/s (that would represent v_s -v_o following Bowers formulation).

Figure 22 and 23 also show their fitting correlation parameters and their respective equations obtained with this power-law regression. These coefficients in the respective regression equations are used as inputs for Equations 18 ($\boldsymbol{a_5}$ & $\boldsymbol{a_6}$) and 19 ($\boldsymbol{b_4}$ & $\boldsymbol{b_5}$). The other coefficients in these equations linked with the petrophysical parameters used random values as weights between 0 and 0.2.

The term $\boldsymbol{V_o}$ (related with V_DIFF and VS_DIFF in Figures 22 and 23) are the called mudline velocity, as defined previously, and would represent the term $\boldsymbol{a_1 - a_2\emptyset - a_3C - a_4V_{oil}}$ in Equation 16 and the term $\boldsymbol{b_1 - b_2\emptyset - b_3C}$ in Equation 17 respectively, taking into account the analogy done with the Bowers (1995) formulation. As detailed before, these coefficients were treated like weights and additional calibration factors during the initial stage of the study, considering that coefficients $\boldsymbol{a_5}$ - $\boldsymbol{a_6}$ for the compressional velocity relation and $\boldsymbol{b_4}$ - $\boldsymbol{b_5}$ for the shear velocity relation are obtained through power-law relations (coefficients in regression equation displayed in Figures 22 and 23).

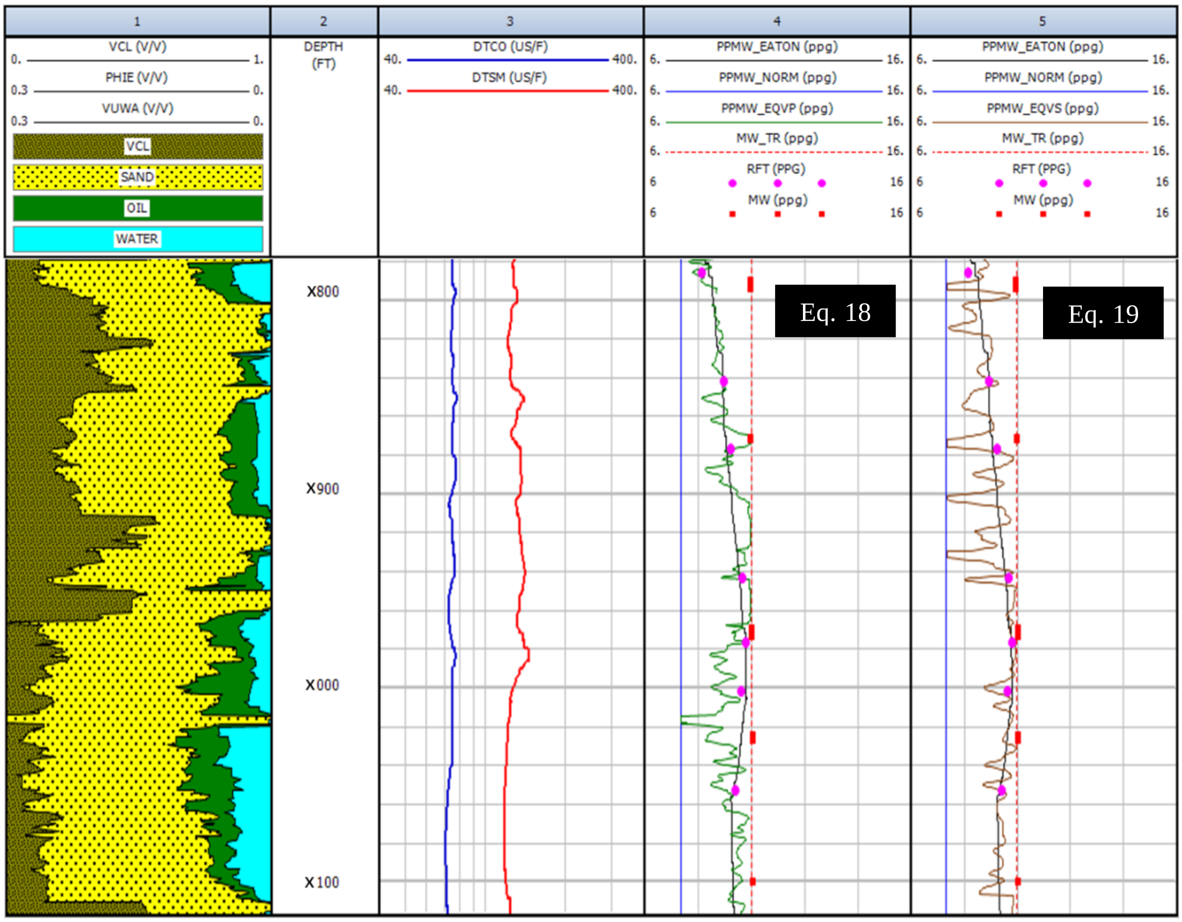

Figure 24: Pore pressure results composite consisting of five tracks, arranged as follows: (1) shading zones for VCL - SAND lithology and WATER – OIL fluids, and interpreted petrophysical data given by PHIE (effective porosity curve), VCL (clay volume) and VUWA (volume of water in the undisturbed zone) in the first track; (2) Relative depths in the second track; (3) Logarithmic compressional slowness (DTCO) and shear slowness (DTSM) in the third track; (4) Hydrostatic pore pressure (PPMW_NORM), Eaton pore pressure (PPMW_EATON), our proposed pore pressure approaches (PPMW_EQVP / PPMW_EQVS) computed directly (see section 4.4.1), direct pore pressure measures (RFT) and mud weight (MW) in the fourth and fifth track respectively.

In Figure 24, we have petrophysical curves of clay volume (VCL), effective porosity (PHIE) and water volume of the undisturbed zone (VUWA) displayed in the second track. The third track shows compressional slowness (DTCO) and shear slowness (DTSM).

The fourth and fifth track in Figure 24 shows hydrostatic pore pressure (PPMW_NORM), Eaton pore pressure (PPMW_EATON), our proposed pore pressure approaches based on compressional and shear relations (Eq. 16 and 17) computed directly or deterministically (section 4.4.1) following a conventional 1D geomechanical processing sequences (PPMW_EQVP / PPMW_EQVS), direct pore pressure measures (RFT) and mud weight (MW) respectively. All pressure curves are in pounds per gallon units (ppg). Both methods used for pore pressure estimation in this figure show good agreement with direct pore pressure measurements. An important difference from the proposed method compared with Eaton is the distribution of pressures along with the shaly sand section intervals, showing a more correlated behavior, considering the variations in lithology, porosity, and fluid effects within the overpressured interval, in contrast with Eaton's estimation. Like other standard MEM-1D processing practices, the Eaton method uses linear interpolation and constant gradient to estimate pore pressure in sand and shaly sand sections. Pore pressure measurements are used for adjustments and calibration, giving rise to uncertainties concerning the actual distribution of pore pressures.

4.5.2 Multidimensional non-linear inversion for calibration

The multidimensional non-linear inversion results using the iterative Levenberg-Marquardt algorithm detailed in section 4.4.2 are applied to this study for calibration purposes in both proposed pore pressure methods. The term "*multidimensional"* is related to the inversion approach of coefficients representing more than 2-dimensional variables including in the formulation (Eq. 16 and 17).

Figure 25 shows the comparative results of proposed pore pressure estimation methods based on VP (fourth track) and VS (fifth track). In each track, the displayed curves are hydrostatic pore pressure (PPMW_NORM), Eaton pore pressure (PPMW_EATON), the proposed approach as in section 4.3.1 (PPMW_EQVP or PPMW_EQVS), the other non-linear calibration proposed approach as detailed in section 4.4.2 (PPMW_EQVP _IN or PPMW_EQVS_IN), direct pore pressure data (RFT) and mud weight (MW). Inversion calibrated results for pore pressure estimation also show a good fit with the direct pore pressure measurements and look in concordance compared with the direct proposed pore pressure method and Eaton. It is observed that the proposed method reflects the lithological and fluid effects in the behavior of the curves taking into account their respective equations.

Additional information like geological structural and stratigraphic interpretation, time migration history analysis, permeability curves, and other reservoir engineering aspects of the formation can be integrated in this kind of pore pressure estimation study to determine the possibility of broken barriers as pore pressure tend to stabilize during geological times (geopressures in equilibrium in consolidated tight formations). This last point is important considering that geomechanical 1D pore pressure estimation assumes this equilibrium for sand zones crossing thin shale layers. Eaton curve reflects this fluid-formation equilibrium assumption during the 1D MEM construction.

Coefficients	A1 = 3.44	A2 = -0.73	A3 = 0.22	A4 = 1.03	A5 = 0.71	A6 = 0.05
Std. Errors	1091.22	0.13	0.02	0.19	1087.74	86.42

Table 7: Output computed coefficients and standard errors for each inverted coefficient.

As a matter of quality inversion indicator, Table 7 shows the inverted coefficients from Equation 16 and their respective standard errors computed from the covariance matrix through the compressional to pore pressure velocity model. In this case, consider the standard error as the extent to which our estimate can vary around its true value or, in other words, can be referred as levels of uncertainty in the obtained coefficient. Analogously, Table 8 shows the same for Equation 17 (shear to pore pressure velocity model). Coefficients with the higher standard errors in the sampling distribution values mean that their values have a broad range of variability during the inversion. In both equations, the coefficient that multiplies the power-law term in the velocity model Equations 16 and 17 (A5 and B4, respectively) gave this uncertainty level as observed in Tables 7 and 8.

Coefficients	B1 = 2.35	B2 = -0.77	B3 = 0.29	B4 = -34.6	B5 = 22.1
Std. Errors	0.03	0.25	0.06	2874.85	31.2

Table 8: Output computed coefficients and standard errors for each inverted coefficient.

Considering some standard error ambiguities obtained in the inverted coefficients as observed in Table 7 and 8, was also computed a root mean square error (*rmse*) in order to compare and evaluate the measured compressional and shear velocities with the modeled results through Equation 16 and 17 using the following expression

$$rmse = (\frac{1}{N}\sum_{1}^{N}(V_M - V_E)^2)^{1/2}, \quad (57)$$

where N is the total number of data, V_M is the measured compressional or shear velocity and V_E is the estimated compressional or shear velocity through Equation 16 and 17, respectively. Table 9 shows the RMSE with low values, giving us good confidence for the non-linear inversion results.

Through Figure 26, we can observe a good agreement between measured velocities (VP_KM / VS_KM) and modeled velocities (VP_KM_POINTVP / VS_KM_POINTVP) with the non-linear inverted LMA approach. Also note in this figure that modeled shear velocity shows a better agreement with the measured data (low *rmse*), which can be related to the faster convergence and stability during the inversion (the VS equation has fewer parameters than the VP equation).

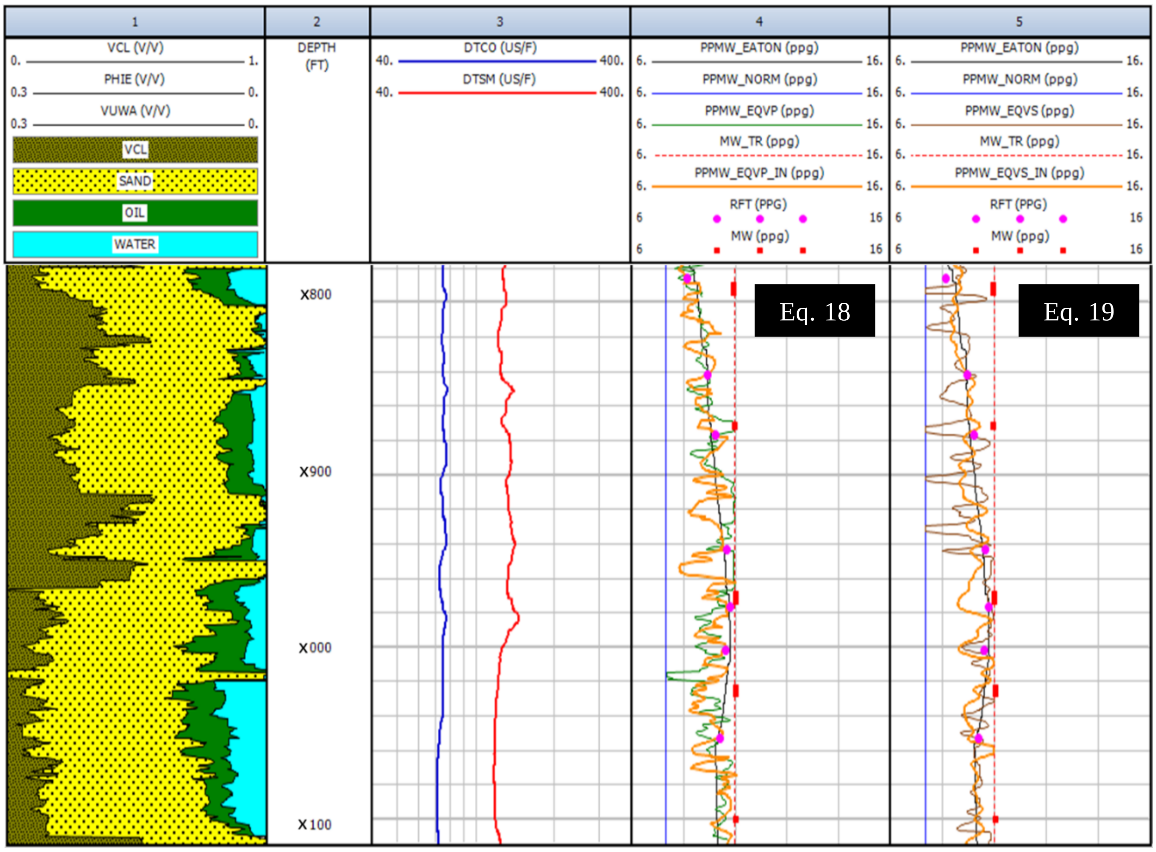

Figure 25: Final pore pressure results composite consisting of five tracks, arranged as follows: (1) shading zones for VCL - SAND lithology and WATER – OIL fluids, and interpreted petrophysical data given by PHIE (effective porosity curve), VCL (clay volume) and VUWA (volume of water in the undisturbed zone) in the first track; (2) Relative depths in the second track; (3) Logarithmic compressional slowness (DTCO) and shear slowness (DTSM) in the third track; (4) Hydrostatic pore pressure (PPMW_NORM), Eaton pore pressure (PPMW_EATON), our proposed pore pressure approaches computed deterministically following section 4.4.1 (PPMW_EQVP / PPMW_EQVS), our proposed pore pressure approaches computed using a non-linear inversion method for calibration (PPMW_EQVP_IN/ PPMW_EQVS_IN), direct pore pressure measures (RFT) and mud weight (MW) in the fourth and fifth track respectively.

	Vp	Vs
RMSE	0.23	0.22

Table 9: RMSE (units values) obtained through the measured velocities and the modeled velocities using the non-linear inverted coefficients in Equations 16 and 17.

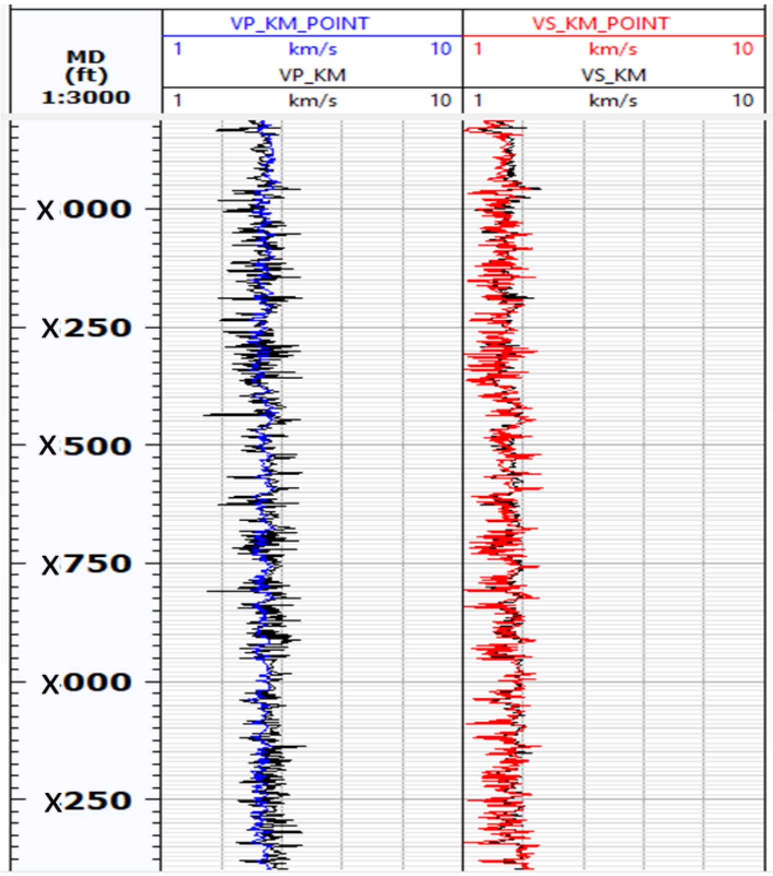

Figure 26: Comparison between measured velocities (VP_KM and VS_KM) and modeled velocities (VP_KM_POINT and VS_KM_POINT) using and non-linear inverted coefficients within Equations 16 and 17 in the respective interval of interest.

5. DISCUSSION, CONCLUSIONS AND RECOMMENDATIONS

The pore pressure predicted by the most used conventional effective stress methods as Eaton’s and Bowers, even if applicable, are not always exact and include ambiguities related to the velocity data and effects of rock property variations. Therefore, it is vital to have an alternative methodology that integrates all relevant petrophysical data to mitigate the uncertainties.

The simplified approach to compute the dry moduli coupled with Gassmann fluid substitution procedure, involving the Doyen and Eberhart-Phillips calibrated with dry rocks measures, provides a link for better understanding how differential pressures, porosity, clay content, and oil saturation affect the compressional velocities responses. Based on this analysis, I propose a new velocity–effective stress relation model to compensate the petrophysical ambiguities during the velocity to pore pressure transformation. It must be highlighted that rock physics tools like fluid substitution are common practice for seismic velocity inversion works and also for seismic pore pressure calibration using laboratory ultrasonic data when available (Dvorkin et al., 2002). However, for MEM 1D construction, calibrations have been traditionally done using direct pore pressure measures in the borehole with sonic velocities and effective stress relations (Bowers, 1995).

The first proposed equation to estimate pore pressure integrates compressional wave velocity, density (overburden), porosity, clay content, and fluid volumes, extending a widely used empirical formula relating velocity with effective stress called the Bowers method. The proposed formulation follows the same lines of the extension proposed by Doyen et al. (2004), including an additional saturation-dependent term to account for the velocity uncertainties related to fluids presence.

The second proposed equation to estimate pore pressure integrates shear-wave velocity, density (overburden), porosity, and clay content, as also an extension of the Bowers method (1995) as done with the previous compressional equation, following the same extension approach proposed by Doyen et al. (2004). This other pore pressure relation as a function of shear velocity and lithology gives us an additional and alternative way for pore pressure prediction with less uncertainty, considering that, at low frequencies, shear velocity is not influenced by fluids.

We also used Eaton's method to predict pore pressure to compare results with the proposed approaches. Both methods used for pore pressure estimation in a consolidated upper cretaceous shaly sand oil reservoir show consistent agreement with direct pore pressure measurements and mud weight data. However, it is important to consider that abnormal pressure observed in this field is linked with compaction disequilibrium as the dominant overpressure mechanism (loading mechanical mechanism dominant). A relevant difference to note in this case study is the distribution of pore pressures along the shaly sand section interval, showing a correlated behavior in the overpressured interval in terms of lithological and petrophysical changes when using our proposed methods. As additional and future discussions, these local effects and behaviors of pore pressure distribution must be studied considering the geological deposition history, fluid migration analysis, and lithology and petrophysical heterogeneities to assert the existence of tight porosity without fluid influx. It must also be emphasized that these calibration coefficients used in the proposed equation can be adjusted or fitted within the direct measurements for a more stabilized behavior of the pore pressure curve considering MEM 1D pore pressure common practices during their construction (following geological burial times) define an equilibrium state of overpressure zones between sands and their adjacent shale layers yielding homogenous pore pressure behaviors.

In order to compare the results obtained with the conventional step process of pore pressure transformation, a multidimensional non-linear inversion sequence approach is implemented to obtain a calibrated set of coefficients included in the proposed equations using pore pressure measurements like RFT (*repeat formation test*) data. The resulting pore pressure values using this non-linear process of calibration also display a consistent behavior with the measured pore pressure data and the other estimation approaches, which are the direct (deterministic calibration) and Eaton method.

Both seismic-based pore pressure calculations and predrill pore pressure predictions from seismic velocities to pore pressure transform can employ the proposed equations and pore pressure computation approach to reduce petrophysical and fluid uncertainties during the pore pressure cube transformation.

It is known that adequate pore pressure estimation results depend on a combination of quality field velocity information and pore-pressure measurements. This requires the use of solid operational procedures, acquisition tools and reliable technologies. As a recommendation for future works, I suggest using stochastic analysis to quantify and propagate data uncertainties and prior information in the pore pressure prediction procedure.

Additional and extensions of this research include a non-linear anisotropic inversion and sonic log correction approach section, considering that velocity data used during pore pressure transformations can be highly affected by VTI anisotropy for the case of deviated wells. This work proposes a practical way of compensating these effects in compressional and shear velocities. The implemented anisotropy inversion method used a BFGS non-linear iterative numerical optimization algorithm to obtain all five elastic stiffness coefficients that fully characterize a VTI medium following Hooke’s law. A synthetic VTI data of two wells are used to estimate three elastic stiffness parameters, penetrating a homogenous shale section at different angles. The inversion done with this synthetic data used P-wave logs at a range of borehole angles to invert the stiffness coefficients that are inputs to estimate final anisotropy Thomsen parameters ε and δ (Thomsen, 1986). These final anisotropy Thomsen parameters are used to correct (verticalize) the final vertical P-wave velocity. This methodology has a significant impact in terms of sonic correction data to get reliable velocities that are very important for seismic processing and geomechanical applications like pore pressure prediction, elastic and mechanical characterization. Results are in concordance with the reference surveys used during this implementation, showing us how the anisotropy can affect the borehole sonic velocities and also these effects can be corrected efficiently using the proposed inversion approach.

Recommendations for future studies, deeper analysis, and improvement of the algorithms in this anisotropy subject must include a complete public data set of an advanced monopole compressional, shear cross dipole, and shear Stoneley data with a good range of borehole angle deviation crossing a VTI medium.

6. REFERENCES

ALI A. H. A., BROWN T., DELGADO R., LEE D., PLUMB D., SMIRNOV N., MARSDEN J. R., PRADO-VELARDE E., RAMSAY L., SPOONER D., STONE T., & STOUFFER T (2003). Watching rocks change-mechanical earth modeling. Oilfield Review, summer, 15, 22-39.

ALFORD, R. M. (1986). Shear data in the presence of azimuthal anisotropy: Dilley, Texas. In SEG Technical Program Expanded Abstracts 1986 (pp. 476-479). Society of Exploration Geophysicists.

AULD, B. A. (1990). Acoustic elds and waves in solids. *RE Krieger*

ARMSTRONG P., IRESON D., CHMELA B., DODDS K., ESMERSOY C., HORNBY B., LEANEY S., SAYERS C., SCHOENGBERG., LYNN H. (1994). The promise of elastic anisotropy.–Oilfield Rev., 6: 36–47.

BANIK, N.C. (1984), Velocity anisotropy of shale sand depth estimation in the North Sea basin: Geophysics, 49, 1411–1419.

BATZLE, M. & WANG, Z. (1992), Seismic properties of pore fluids. Geophysics, 57, 1396–1408.

BOWERS, G. L. (1995). Pore pressure estimation from velocity data: Accounting for overpressure mechanisms besides undercompaction. SPE Drilling & Completion, 10(02), 89-95.

BOWERS, G.L. (1999). State of the Art in Fracture Gradient Estimation. DEA Project, 119.

BOWERS, G. L. (2002). Detecting high overpressure. The leading edge, 21(2), 174-177.

BRUCE B. & BOWERS G. L. (2002). Pore pressure terminology. The Leading Edge, 21(2), 170-173.

BRIE, A., ENDO, T., VALERO, H.P., UCHIYAMA, T., SKELTON, O. (2000). Best slowness determination from sonic waveforms. In EAGE Conference on Exploring the Synergies between Surface and Borehole Geoscience-Petrophysics meets Geophysics (pp. cp-19). European Association of Geoscientists & Engineers.

BROWN, J.S., & KORRINGA, J. (1975), On the elastic properties of a porous rock on the compressibility of the pore fluid: Geophysics, 40, 608– 616.

CASTAGNA, J. P., BATZLE, M. L. & EASTWOOD R. L. (1985). Relationship between compressional wave and shear wave velocities in clastic silicate rocks: Geophysics, V. 50, 571 - 581.

CARCIONE, J. M., HELLE, H. B., PHAM, N. H. & TOVERUD, T. (2003). Pore pressure estimation in reservoir rocks from seismic reflection data. Geophysics, Volume 68, Issue 5, 1569-1579.

DICKINSON, G. (1953). Geological aspects of abnormal reservoir pressures in Gulf Coast Louisiana. AAPG Bulletin, 37(2), 410-432.

DOYEN, P. M., MALINVERNO, A., PRIOUL, R., HOOYMAN, P., NOETH, S., BOER, L. PSAILA, D., SAYERS, C. M., SMIT, T. J. H., EDEM, C. & WERVELMAN, R. (2004). Seismic pore pressure prediction with uncertainty using a probabilistic mechanical earth model. In SEG Technical Program Expanded Abstracts 2004 (pp. 1366-1369). Society of Exploration Geophysicists.

DUIJNDAM, A. J. W. (1988). Bayesian estimation in seismic inversion, part I: Principles: Geophysical Prospecting, 36, 878–898.

DUTTA, N. C. (2002). Geopressure prediction using seismic data: Current status and the road ahead. Geophysics, 67(6), 2012-2041.

DVORKIN, J. (2002). Pore pressure and fluid detection from compressional-and shear-wave data. In EAGE/SEG Research Workshop on Reservoir Rocks-Understanding reservoir rock and fluid property distributions-measurement, modelling and applications. https://doi. org/DOI (Vol. 10, pp. 2214-4609).

DVORKIN, J., MAVKO, G., NUR, A. (2002). Method for overpressure detection from compressional- and shear-wave data. United States Patent no 6,374,186.

EATON, B. A. (1975). The equation for geopressure prediction from well logs. Presented at 50th Annual Fall Meeting of the Society of Petroleum Engineers of AIME, 5544.

EBERHART-PHILLIPS D., HAN D. & ZOBACK M. (1989). Empirical relationships among seismic velocity, effective pressure, porosity, and clay content in sandstone. Geophysics, 54(1), 82-89.

ELLIS, R. G., AND OLDENBURG, D. W. (1994). Applied geophysical inversion: Geophysical Journal International, 116, 5–11.

FERTL W. H. AND CHILINGARIAN G. V. (1977). Importance of Abnormal Formation Pressures (includes associated paper 6560). Journal of Petroleum Technology, 29(04), 347-354.

FLETCHER, R. (1971). A modified Marquardt subroutine for nonlinear least squares, Atomic Energy Research Establishment.

FLETCHER, R. (1987). Practical methods of optimization (2nd ed.), New York: John Wiley & Sons, ISBN 978-0-471-91547-8

FOSTER, J. B., & WHALEN, J. E. (1966). Estimation of formation pressures from electrical surveys-offshore Louisiana. Journal of Petroleum Technology, 18(02), 165-171.

FURRE, A., AND BREVIK, I. (1998). Characterization of angle dependency in sonic logs. In SEG Technical Program Expanded Abstracts 1998 (pp. 292-295). Society of Exploration Geophysicists.

GAVIN, H. (2011). The Levenberg-Marquardt method for nonlinear least squares curve-fitting problems. Department of Civil and Environmental Engineering, Duke University, 28, 1-5.

GOLDBERG, I.. & GUREVICH, B. (1998). A semi-empirical velocity porosity-clay model for petrophysical interpretation of P- and S-velocities. Geophysical Prospecting 46, 271-285.

HAN D., NUR A. & MORGAN D., 1986, Effects of Porosity and Clay Content on Wave Velocities in Sandstones. Geophysics, vol 51.

HOLZBERG, B. B. (2005). Probabilistic Pore Pressure Prediction in Reservoir Rocks Through Compressional and Shear Velocities. Ph.D. Dissertation, Catholic University of Rio de Janeiro, PUC-Rio (in Portuguese).

HORNBY, B. E. (1995). The elastic properties of shales: Ph.D. thesis, Univ. Cambridge.

HORNBY, B. E. (1998). Experimental laboratory determination of the dynamic elastic properties of wet, drained shales: J. Geophys. Res., 103, No. B4, 29945–29964.

HORNBY, B. E., HOWIE, J. M., & INCE, D. W. (2003). Anisotropy correction for deviated-well sonic logs: Application to seismic well tie. Geophysics, 68(2), 464-471.

HOTTMANN, C. E. & JOHNSON, R. K. (1965). Estimation of formation pressures from log-derived shale properties: Journal of Petroleum Technology, 17, 717–722, DOI: 10.2118/1110-PA.

HOWS, A. M., HOFMANN, R., AND GONZALEZ, E. F. (2013). Characterization of anisotropic dynamic mechanical rock properties in shale gas plays. In 47th US Rock Mechanics/Geomechanics Symposium. OnePetro.

JIN Y., WANG., LI Z. (2000). Undercompaction Causes for Using Seismic Data to Predict Formation Pore Pressure. Petroleum Drilling Techniques, (3): 7-9

JONES, L. E. A., AND WANG, H. F. (1981). Ultrasonic velocities in Cretaceous shales from the Williston Basin: Geophysics, 46, 288–297.

KAN, T. K. & SWAN, H. W. (2001). Geopressure prediction from automatically-derived seismic velocities: Geophysics, 66, 1937–1946, DOI: 10 .1190/1.1487135.

LANE, R. A., & MACPHERSON, L. A. (1976). A review of geopressure evaluation from well logs-Louisiana Gulf Coast. Journal of petroleum technology, 28(09), 963-971.

LAW B. & SPENCER C. W. (1998). Abnormal Pressure in Hydrocarbon Environments. Abnormal Pressure in Hydrocarbon Environments, chapter 1, AAPG Memoir 70, 1-11.

LEVENBERG, K. (1944). A Method for the Solution of Certain Non-Linear Problems in Least Squares. Quarterly of Applied Mathematics. 2 (2): 164–168. doi:10.1090/qam/10666.

LEWIS, A. S. & OVERTON, M. L. (2008). Nonsmooth optimization via BFGS. Submitted to SIAM J. Optimiz, 1-35.

MALINVERNO, A., SAYERS, C. M., WOODWARD, M. J. & BARTMAN, R. C. (2004). Integrating diverse measurements to predict pore pressure with uncertainties while drilling: SPE Annual Technical Conference and Exhibition, SPE, Extended Abstracts, DOI: 10.2118/90001-MS.

MARQUARDT, D. (1963). An Algorithm for Least-Squares Estimation of Nonlinear Parameters. SIAM Journal on Applied Mathematics. 11 (2): 431–441. doi:10.1137/0111030.

MARTINSEN, R. S. (1994). Summary of Published Literature on Anomalous Pressures: Implications for the Study of Pressure Compartments. AAPG Memoir 61.

MASCARENHAS, W. F. (2004). The BFGS method with exact line searches fails for non-convex objective functions. Mathematical Programming 99(1): 49-61.

MATTHEWS, W. R., & KELLY, J. (1967). How to predict formation pressure and fracture gradient, The Oil and Gas Journal.

MAVKO, G., MUKERJI, T. & DVORKIN, J. (1998). The Rock Physics Handbook: Tools for Seismic Analysis in Porous Media. Cambridge University Press, United Kingdom.

MILLER, D. E., & CHAPMAN, C. H. (1991). Incontrovertible evidence of anisotropy in cross-well data: 61st Ann. Intenat. Mtg., Soc. Expl. Geophys., Expanded Abstracts, 825–828.

MOUCHET J. P. & MITCHELL A. (1989). Abnormal pressures while drilling: origins, prediction, detection, evaluation (Vol. 2). Editions Technip.

NAYFEH A. H. (1995). Wave propagation in layered anisotropic media with applications to composites. Elsevier Science, North-Holland series in Applied Mathematics and Mechanics, Vol. 39, 1995.

NUNEZ-IGLESIAS, J., VAN DER WALT, S., DASHNOW, H. (2017). Elegant SciPy: The Art of Scientific Python. O'Reilly. ISBN 978-1-4919-2287-3..

OUGHTON, R. H., WOOFF, D. A., HOBBS, R. W., SWARBRICK, R. E. & O'CONNOR, S. A. (2018). A sequential dynamic Bayesian network for pore pressure estimation with uncertainty quantification, Geophysics, 83 (2), D27-D39.

PENNEBAKER, E. S. (1968). An engineering interpretation of seismic data. In Fall Meeting of the Society of Petroleum Engineers of AIME. OnePetro

PLUMB, R. A., EDWARDS, S., PIDCOCK, G. & LEE, D. (2000). The Mechanical Earth Model Concept and its Application to High Risk Well Construction Projects: SPE 59128.

ROCHA, L. A. S., AZEVEDO, C. T. (2009). Projetos de poços de petróleo: geopressões e assentamentos de colunas de revestimentos, 2.ed., Rio de Janeiro: Ed. Interciência, Petrobras.

SAYERS, C.M., SMIT, T.J.H., VAN EDEN C., WERVELMAN, R., BACHMANN, B., FITTS, T., BINGHAM, J., MCLACHLAN, K., HOOYMAN, P., NOETH, S. & MANDHIRI, D. (2003). Use of reflection tomography to predict pore pressure in overpressured reservoir sands. In SEG Technical Program Expanded Abstracts 2003 (pp. 1362-1365). Society of Exploration Geophysicists..

SAYERS C. M., WOODWARD, M. J. & BARTMAN R. C. (2002). Seismic pore-pressure prediction using reflection tomography and 4-C seismic data. The Leading Edge, 21(2), 188-192.

SEN, M. K., & STOFFA, P. L. (1995). Global optimization methods in geophysical inversion: Elsevier.

SNYMAN, J. A., WILKE, D. N. (2018). Practical Mathematical Optimization : Basic Optimization Theory and Gradient-Based Algorithms (2nd ed.). Berlin: Springer. ISBN 978-3-319-77585-2.

SMITH, T. M., SONDERGELD, C. H., & RAI, C. S. (2003). Gassmann fluid substitutions: A tutorial, Geophys., 68, 430.

SWARBRICK, R. E., OSBORNE, M. J. (1994). Mechanisms that generate abnormal pressure: an overview. AAPG Memoir 70.

TARANTOLA, A. (2004). Inverse problem Theory and Methods for Model Parameter Estimation. SIAM

TERZAGHI, K.. (1973). Theoretical Soil Mechanics: New York, John Wiley & Sons, Inc.

THOMSEN, L. (1986). Weak elastic anisotropy: Geophysics 51, 1954–1966.

TOSAYA, C., & NUR, A. (1989). Effects of diagenesis and clays on compressional velocities in rocks, in Nur, A., and Wang, Z., Eds., Seismic and acoustic velocities in reservoir rocks: Soc.Expl.Geophys.,116– 119.

TRAUGOTT, M. O. (1997). Pore/fracture pressure determinations in deep water. World Oil, 218(8), 68-70.

WALSH, J., SINHA B., PLONA T., & MILLER D. (2007). Derivation of anisotropy parameters in a shale using borehole sonic data. In SEG Technical Program Expanded Abstracts 2007 (pp. 323-327). Society of Exploration Geophysicists.

WANG, Z. (2001). Fundamentals of seismic rock physics: Geophysics, 66, 398–412.

WHITE, J. E., MARTINEAU-NICOLETIS, L., & MONASH,C. (1989). Measured anisotropy in Pierre Shale, in Nur, A., and Wang, Z., Eds., Seismic and acoustic velocities in reservoir rocks: Soc.Expl.Geophys.,374– 390.

ZHU J., ZHANG X., ZHANG G. (2011). A Study of Abnormal Pressure Distribution and Formation Mechanism in Qiongdongnan Basin. Natural Gas Geoscience, (2): 324-330.

ZIJIAN C., JINGEN D., BAOHUA Y., QIANG T., ZHUO C. (2015). The Improvement Methods of Pore Pressure Prediction Accuracy in the Central Canyon in Qiongdongnan Basin, 4th International Conference on Environmental, Energy and Biotechnology Volume 85 of IPCBEE, DOI:10.7763/IPCBEE. V85. 1

ZOBACK, M. D. (2010). Reservoir Geomechanics (Pbk. ed.). Cambridge: Cambridge University Press. ISBN 978-0521146197